Low-Frequency Variability in the Midlatitude Atmosphere Induced by an Oceanic Thermal Front

YIZHAK FELIKS,* MICHAEL GHIL,+ AND ERIC SIMONNET#

Department of Atmospheric Sciences, and Institute of Geophysics and Planetary Physics, University of California, Los Angeles, Los Angeles, California

(Manuscript received 30 October 2002, in final form 3 October 2003)

ABSTRACT

This study examines the flow induced in a highly idealized atmospheric model by an east–west-oriented oceanic thermal front. The model has a linear marine boundary layer coupled to a quasigeostrophic, equivalent-barotropic free atmosphere. The vertical velocity at the top of the boundary layer drives the flow in the free atmosphere and produces an eastward jet, parallel to the oceanic front's isotherms. A large gyre develops on either side of this jet, cyclonic to the north and anticyclonic to the south of it. As the jet intensifies during spinup from rest, it becomes unstable. The most unstable wave has a length of about 500 km, it evolves into a meander, and eddies detach from the eastern edge of each gyre.

The dependence of the atmospheric dynamics on the strength T_* of the oceanic front is studied. The Gulf Stream and Kuroshio fronts correspond roughly, in the scaling used here, to $T_* \cong 7$°C. For weak fronts, $T_* \leq 4$°C, the circulation is steady and exhibits two large, antisymmetric gyres separated by a westerly zonal jet. As the front strengthens, $4 < T_* < 5$, the solution undergoes Hopf bifurcation to become periodic in time, with a period of 30 days, and spatially asymmetric. The bifurcation is due to the westerly jet's barotropic instability, which has a symmetric spatial pattern. The addition of this pattern to the antisymmetric mean results in the overall asymmetry of the full solution. The spatial scale and amplitude of the symmetric, internally generated, and antisymmetric, forced mode increase with the strength T_* of the oceanic front. For $T_* \geq 5$°C, the solution becomes chaotic, but a dominant period still stands out above the broadband noise. This dominant period increases with T_* overall, but the increase is not monotonic.

The oceanic front's intensity dictates the mean speed of the atmospheric jet. Two energy regimes are obtained. 1) In the low-energy regime, the SST front, and hence the atmospheric jet, are weak; in this regime, small meanders develop along the jet axis, and the dominant period is about 25 days. 2) In the high-energy regime, the SST front and the jet are strong; in it, large meanders and eddies develop along the jet, and the dominant oscillation has a period of about 70 days. The physical nature of the two types of oscillations is discussed, as are possible transitions between them when T_* changes on very long time scales. The results are placed in the context of previous theories of ocean front effects on atmospheric flows, in which baroclinic phenomena are dominant.

1. Introduction

Over the last two decades, the response of the atmospheric marine boundary layer (AMBL) to oceanic fronts has been studied in observations, as well as by analytical and numerical models (Sweet et al. 1981; Businger and Shaw 1984; Hsu 1987; Rogers 1989; Warner et al. 1990; Doyle and Warner 1990, 1993; Giordani and Planton 2000). These studies have shown that the AMBL reaches heights of 600–1200 m, with the greater height lying over the warm side of the front. The potential temperature gradient of the induced atmospheric front in many cases extends up to the top of the AMBL. The vertical velocity at the top of the AMBL right above the front's axis reaches values of several centimeters per second, while the horizontal wind along the front has a speed of several meters per second. The maximum wind speed is collocated with the pressure gradient maximum.

The circulation in the AMBL adjusts to changes in the oceanic surface conditions in several hours. In the case of very strong fronts, as observed in the Genesis of Atlantic Lows Experiment (GALE) program (Doyle and Warner 1990), intense and narrow jets have been

* Permanent affiliation: Mathematics Department, Israel Institute of Biological Research, Nes-Ziona, Israel.

+ Additional affiliation: Département Terre-Atmosphère-Océan, Ecole Normale Supérpieure, and Laboratoire de Météorologie Dynamique du CNRS, Paris, France.

Permanent affiliation: Institut Non-Linéaire de Nice, CNRS, Nice, France.

Corresponding author address: Michael Ghil, Dept. of Atmospheric Sciences and Institute of Geophysics and Planetary Physics, University of California, Los Angeles, Los Angeles, CA 90095-1567. E-mail: ghil@atmos.ucla.edu

measured whose speed exceed 20 m s^{-1}. Superimposed on the jets were short waves of 50–90 km and small atmospheric eddies. These waves and eddies have been attributed to barotropic instability induced by the horizontal shear (Doyle and Warner 1993).

The most prominent inhomogeneity in ocean surface properties is the thermal contrast across major oceanic currents and upwelling zones. Midoceanic thermal fronts, such as the Gulf Stream and Kuroshio Extension, are permanent features of the midlatitude ocean circulation (Stommel 1965; Stommel and Yashida 1972; Robinson 1983). These fronts change in position and strength on the time scale of weeks to years. The sea surface temperature (SST) difference across these fronts is of about 4°–10°C (100 km)$^{-1}$. Most of the data on these fronts are derived from a limited number of in situ hydrographic sections and a much larger number of remotely taken satellite infrared images (Lee and Cornillon 1996).

There are thus two types of atmospheric low-frequency variability (LFV) that can be induced by oceanic fronts. First, their slow changes in position and intensity can directly force similar changes in the atmospheric surface fronts they induce, and hence in the free atmosphere above. Second, the atmospheric response to a steady oceanic front might not be steady and thus generate LFV even when the oceanic forcing is constant. This second possibility has not been explored in previous LFV studies or even in studies of the midlatitude coupled ocean–atmosphere system (Saravanan and McWilliams 1995; Neelin and Weng 1999; Weng and Neelin 1999; Gallego and Cessi 2001). Previous lack of attention to atmospheric LFV induced by fixed oceanic fronts is mainly due to the fact that, even in coupled general circulation model (GCM) studies, the grid size of the atmospheric GCM was typically 200–500 km, that is, much larger than the cross-frontal scale of about 100 km.

Intraseasonal oscillations of 40–50 days were first observed in the tropical atmosphere by Madden and Julian (1971) and many studies of such oscillations since then have been reviewed by Madden and Julian (1994). Midlatitude oscillations with both shorter and longer periods were described by Branstator (1987), Kushnir (1987), Dickey et al. (1991), Ghil and Mo (1991a,b), and Plaut and Vautard (1994). Several theoretical and modeling studies attribute midlatitude oscillations with periods of 15–40 days to the interaction of the jet stream with high mountain ranges such as the Rocky Mountains and the Himalayas (Jin and Ghil 1990; Ghil and Robertson 2000; Keppenne et al. 2000), while others attribute it to the barotropic instability of the zonally asymmetric climatological mean flow (Simmons et al. 1983). Lott et al. (2001, 2004a,b) have provided observational evidence for the role of mountain torques in 15–30-day oscillations in the Northern Hemisphere. Plaut and Vautard (1994), on the other hand, found prominent 35- and 70-day oscillations over the Atlantic Ocean, where mountain torques are unlikely to play a major role.

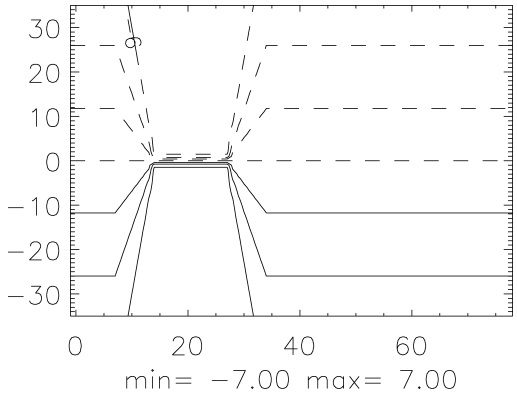

FIG. 1. The prescribed SST pattern for a finite-length front with strength $T_a = 3.5$°C and frontal-width parameter $d = 50$ km [see Eqs. (24) and (25)]. Contour interval (CI) is 2°C, starting at ±1°C; positive contours are solid; negative and zero contours dashed. The front lies along the x axis, is 600 km long, and is centered at $x = 1000$ km. All spatial patterns are shown for the same rectangular domain of 4000 km × 3500 km; axes in nondimensional units, to be multiplied by $L = 50$ km to obtain the dimensional coordinates of position.

In this study we examine the direct influence of long and narrow oceanic fronts—that is, fronts for which the ratio between the cross-frontal width and the zonal extent is small, like the Gulf Stream in the Atlantic and the Kuroshio Extension in the Pacific—on the AMBL and the free atmosphere above it. In so doing, we find that these fronts can give rise to atmospheric LFV. The time scale that interests us is thus longer than a week, while previous studies concentrated on steady-state AMBL solutions (Hsu 1987) or on the AMBL's short-time evolution (of the order of 12–24 h).

An east–west-oriented surface thermal front of finite zonal extent is shown in Fig. 1. The anticipated atmospheric circulation in its presence can be depicted as follows. Let us assume that the cold water lies to the north of the front. Thus the cold air also lies to the north and the warm air to the south of it. The wind near the sea surface blows therefore from north to south.

The maximum wind speed is obtained over the line segment of maximum thermal gradient, in the middle of the SST front, and decays toward its edges. Thus, horizontal flow diverges north of the front and converges south of it. Consequently, there is a downward flow north of the front and an upward flow south of it. The resulting flow in a meridional plane perpendicular to the front spins up an eastward geostrophic jet. As this jet strengthens, it becomes unstable. We study here the evolution of the entire atmospheric flow that is affected by the eastward jet and its instabilities.

Note that the traditional approach to changes induced in the midlatitude atmospheric circulation by SST anomalies emphasizes shallow baroclinic phenomena; see for instance the review by Kushnir et al. (2002). These baroclinic effects are entirely absent from our model and we

return to a discussion of the broader context in our concluding section.

In section 2 the atmospheric model is described. Section 3 deals with an approximate steady-state circulation, while in section 4, we study its instabilities and the LFV so obtained. In section 5, we summarize and discuss these results and their possible implications for the study of atmospheric variability induced by SST fronts.

2. The atmospheric model

The atmospheric model we use is composed of a steady-state analytical AMBL and a time-dependent numerical model for the free atmosphere above it. These two models are presented in the next two sections.

a. The atmospheric marine boundary layer model

The AMBL takes only several hours to adjust to the large-scale environmental conditions. This relaxation time is much shorter than the characteristic atmospheric and oceanic times, of weeks to years, in which we are interested here. We assume, therefore, that the AMBL is in instantaneous equilibrium with the oceanic front's SST field (Sweet et al. 1981), whether the latter itself is steady or slowly varying. In the present section 2a and throughout sections 3, 4a, and 4b, we take the SST anomaly field to be steady, $T = T(x, y)$, while in the section 4c it will be periodic, $T = T(x, y, t) = T(x, y, t + P)$, with period P longer than a year. Thus, we shall take the perturbation θ in the AMBL's virtual potential temperature, at height $z = 0$, to equal T throughout this paper.

In the AMBL's frontal region the cold air from the north blows southward across the front, and results in a well-mixed AMBL. This yields an almost constant profile of the virtual potential temperature throughout the mixed layer, up to its height H_E, with $\theta(z) \cong \theta(0) = T$.

The pressure perturbation in the AMBL, at an arbitrary horizontal location (x, y), is thus found from the hydrostatic equation, combined with the equation of state:

$$\frac{1}{\rho_0}\frac{\partial p}{\partial z} = -\frac{g\rho}{\rho_0} = \frac{g\theta}{\theta_0}. \tag{1}$$

Integrating Eq. (1) from an arbitrary height z within the AMBL to its top H_E yields

$$\frac{p(z)}{\rho_0} = \frac{p(H_E)}{\rho_0} - \frac{g}{\theta_0}\int_z^{H_E} \theta(s)\, ds$$

$$= \frac{p(H_E)}{\rho_0} - \frac{g}{\theta_0}(H_E - z)\theta. \tag{2}$$

Here, ρ is the perturbation density, with ρ_0 its reference value, and θ_0 that of θ, while g is the acceleration of gravity, and f is the Coriolis parameter at a central latitude.

TABLE 1. Characteristic scales and reference values for the atmospheric model.

Parameter	Value
L (km)	50
H (km)	10
H_a (km)	7.8
H_E (km)	0.81
T_i (day)	0.58
V (m s^{-1})	1
β_0 (m^{-1} s^{-1})	1.8×10^{-11}
k_0 (m^2 s^{-1})	3.3
K_H (m^2 s^{-1})	10^2
f (s^{-1})	10^{-4}
g (m s^{-2})	9.81
θ_0 (K)	300
ρ_0 (g cm^{-3})	10^{-3}
ϵ	0.2
β	0.045
F_r	0.0112
E_H	8.0×10^{-4}
α	110.43
γ	0.086

The height H_E of the AMBL is given by $H_E = \pi(2k_0/f)^{1/2}$, where k_0 is the turbulent eddy diffusion coefficient in the vertical direction (Holton 1992), and $p(H_E)$ is the pressure perturbation at the top of AMBL. We neglect herewith the difference in height between the top of the AMBL over the cold and the warm side of the front. This difference is small near the SST front since the cold air flows over the warm water; as a result, the atmospheric column is destabilized, yielding a thick AMBL over the cold side of the oceanic front too. The difference will only be large far away from the SST front, and we plan to take this difference into account in future work (see section 5c).

The horizontal gradient of the pressure perturbation is given by

$$\frac{1}{\rho_0}\frac{\partial p}{\partial x} = \frac{1}{\rho_0}\frac{\partial}{\partial x}p(H_E) - \frac{g}{\theta_0}(H_E - z)\frac{\partial \theta}{\partial x}, \tag{3a}$$

$$\frac{1}{\rho_0}\frac{\partial p}{\partial y} = \frac{1}{\rho_0}\frac{\partial}{\partial y}p(H_E) - \frac{g}{\theta_0}(H_E - z)\frac{\partial \theta}{\partial y}. \tag{3b}$$

The appropriate physical parameters are listed in Table 1. In this section, the variables are dimensional unless explicitly stated otherwise.

The pressure gradient in (3) has two components. One is due to the geostrophic wind in the free atmosphere at the top of the AMBL, that is,

$$fv_G = \frac{1}{\rho_0}\frac{\partial p(H_E)}{\partial x},$$

$$fu_G = -\frac{1}{\rho_0}\frac{\partial p(H_E)}{\partial y},$$

and is independent of z; this is essentially the component

familiar from general boundary layer theory, as in the classical Blasius solution of flow over a plate (Schlichting and Gersten 1999). The second component is due to the thermal oceanic front and it is a function of z.

The linear equations of motion in the AMBL are

$$k_0\frac{\partial^2 u}{\partial z^2} + fv - \frac{1}{\rho_0}\frac{\partial p}{\partial x} = 0, \tag{4a}$$

$$k_0\frac{\partial^2 v}{\partial z^2} - fu - \frac{1}{\rho_0}\frac{\partial p}{\partial y} = 0. \tag{4b}$$

The boundary conditions are

$$u = v = 0 \qquad \text{at } z = 0,$$
$$u = u_G, \quad v = v_G \quad \text{as } z \to \infty. \tag{5}$$

At the top of the AMBL, we also need a condition that assures the continuity of the momentum flux at $z = H_E$, since $\partial/\partial z(\partial p/\partial x, \partial p/\partial y)$ in Eqs. (3a) and (3b) is discontinuous at H_E. The appropriate conditions are

$$u_- = u_+, \qquad v_- = v_+,$$
$$k_0\frac{\partial u}{\partial z_-} = k_0\frac{\partial u}{\partial z_+}, \qquad k_0\frac{\partial v}{\partial z_-} = k_0\frac{\partial v}{\partial z_+}, \tag{6}$$

where the subscripts + and − stand for the limits from above and below $z = H_E$.

The closed-form, analytical solution to Eqs. (4a) and (4b) in the AMBL, using Eq. (3), the boundary and continuity conditions (5) and (6), and geostrophic balance in the free atmosphere, is

$$\begin{aligned}
u(z) &= u_G + \frac{g}{f\theta_0}(H_E - z)\frac{\partial T}{\partial y} - e^{-\pi z/H_E}\left[u_G\cos\left(\frac{\pi z}{H_E}\right) + v_G\sin\left(\frac{\pi z}{H_E}\right)\right] + e^{-\pi z/H_E}\frac{g}{f\theta_0}H_E\left[\frac{\partial T}{\partial x}\sin\left(\frac{\pi z}{H_E}\right) - \frac{\partial T}{\partial y}\cos\left(\frac{\pi z}{H_E}\right)\right] \\
&\quad + \frac{g}{f\theta_0}\frac{H_E}{4\pi e^{\pi}}\left[(e^{\pi z/H_E} - e^{-\pi z/H_E})\left(\frac{\partial T}{\partial x} - \frac{\partial T}{\partial y}\right)\cos\left(\frac{\pi z}{H_E}\right) - (e^{\pi z/H_E} + e^{-\pi z/H_E})\left(\frac{\partial T}{\partial x} + \frac{\partial T}{\partial y}\right)\sin\left(\frac{\pi z}{H_E}\right)\right], \\
v(z) &= v_G - \frac{g}{f\theta_0}(H_E - z)\frac{\partial T}{\partial x} + e^{-\pi z/H_E}\left[u_G\sin\left(\frac{\pi z}{H_E}\right) - v_G\cos\left(\frac{\pi z}{H_E}\right)\right] + e^{-\pi z/H_E}\frac{g}{f\theta_0}H_E\left[\frac{\partial T}{\partial x}\cos\left(\frac{\pi z}{H_E}\right) + \frac{\partial T}{\partial y}\sin\left(\frac{\pi z}{H_E}\right)\right] \\
&\quad + \frac{g}{f\theta_0}\frac{H_E}{4\pi e^{\pi}}\left[(e^{\pi z/H_E} - e^{-\pi z/H_E})\left(\frac{\partial T}{\partial x} + \frac{\partial T}{\partial y}\right)\cos\left(\frac{\pi z}{H_E}\right) + (e^{\pi z/H_E} + e^{-\pi z/H_E})\left(\frac{\partial T}{\partial x} - \frac{\partial T}{\partial y}\right)\sin\left(\frac{\pi z}{H_E}\right)\right],
\end{aligned} \tag{7}$$

where we have assumed that $\theta(x, y, z, t) = T(x, y)$.

Given u and v throughout the AMBL, we obtain the vertical velocity at its top by integrating the continuity equation:

$$\begin{aligned}
w(H_E) &= -\int_0^{H_E}\left(\frac{\partial u}{\partial x} + \frac{\partial v}{\partial y}\right)dz \\
&= \zeta_G\frac{H_E}{2\pi}(1 + e^{-\pi}) \\
&\quad - \frac{gH_E^2}{2\pi f\theta_0}\nabla^2 T\left[1 - \frac{1}{2\pi} + e^{-\pi}\left(1 - \frac{1}{\pi} - \frac{e^{-\pi}}{2\pi}\right)\right];
\end{aligned} \tag{8}$$

here

$$\zeta_G \equiv \frac{\partial v_G}{\partial x} - \frac{\partial u_G}{\partial y}$$

is the vorticity of the geostrophic wind at $z = H_E$, and $\nabla^2 T \equiv (\partial^2/\partial x^2 + \partial^2/\partial y^2)T$ is the Laplacian of the SST field. Thus, the vertical velocity at the top of the AMBL can be approximated by

$$w(H_E) \cong \frac{H_E}{2\pi}\left[\zeta_G - \frac{gH_E}{f\theta_0}\left(1 - \frac{1}{2\pi}\right)\nabla^2 T\right]. \tag{9}$$

This vertical velocity has two components, one due to the geostrophic flow above the AMBL that we call the mechanical component, the other due to the wind induced in the AMBL by the oceanic thermal front that we call the thermal component. For cyclonic flow in the free atmosphere the geostrophic component has a positive sign and for anticyclonic flow a negative one. For an anomaly field that varies like an eigenfunction of the Laplacian (for instance a sinusoid in the zonal direction), the thermal component has a positive sign over warm water (i.e., near an SST maximum) and a negative one over cold water (near an SST minimum). Since these two terms tend to cancel each other (see below, section 3b), one will predominantly find cyclonic flow over cold water and anticyclonic flow over warm water, as expected.

b. The QG model in the free atmosphere

In the free atmosphere above the AMBL, we use a quasigeostrophic (QG) model with a single, equivalent-barotropic mode in the vertical. This mode is described

by the streamfunction $\psi = \psi(x, y, t)$. The model equations are nondimensionalized by the following characteristic scales:

$$X, Y \propto L; \qquad Z \propto H; \qquad T_i \propto L/V; \qquad \psi \propto VL. \quad (10)$$

Here, L is the horizontal length scale across the front, H is the vertical scale of the free atmosphere, T_i is the advective time scale, and V scales the wind speed in the cross-front direction. The appropriate scales are listed in Table 1, along with the main physical parameters. In this section, a star indicates the dimensional variables.

The nondimensional potential vorticity (PV) equation with this scaling is

$$\frac{\partial q}{\partial t} + \beta\frac{\partial \psi}{\partial x} + J(\psi, q) = r_H\nabla^4\psi + \frac{\partial w_a}{\partial z}, \quad (11)$$

where w_a is the vertical velocity in the free atmosphere (Pedlosky 1987; Holton 1992). The relative PV is given by

$$q \equiv \nabla^2\psi - \lambda^2\psi, \quad (12)$$

and the nondimensional parameters β, λ, and r_H by

$$\beta = \beta_0\frac{L^2}{V}, \qquad \lambda = \frac{L}{R_d}, \qquad r_H = \frac{E_H}{2\epsilon} = \frac{K_H}{VL}; \quad (13)$$

β_0 is the meridional gradient of f, R_d is the Rossby radius of deformation of the atmosphere, K_H is the dimensional horizontal diffusion coefficient, $\epsilon = V/fL$ is the Rossby number based on the cross-frontal speed V, and $E_H = 2K_H/fL^2$ is the horizontal Ekman number. Later, we will also use the Froude number $F_r = V(gH_E)^{-1/2}$.

Integrating Eq. (11) with respect to z from $z = 0$ to $z = H_a/H$, the (nondimensional) height of the free atmosphere (see Table 1), and dividing by this height H_a/H, we obtain

$$\frac{\partial q}{\partial t} + \beta\frac{\partial \psi}{\partial x} + J(\psi, q) = r_H\nabla^4\psi - \frac{H}{H_a}w_a(x, y, z = 0, t). \quad (14)$$

The lower boundary condition for the free atmosphere is

$$\frac{H}{H_a}w_a(x, y, z = 0, t) = \frac{1}{\epsilon}\frac{H}{H_a}w\left(\frac{H_E}{H}\right) = \gamma\nabla^2\psi - \frac{\alpha}{\theta_0}\nabla^2T^*, \quad (15)$$

where T^* is the dimensional SST. The dimensional vertical velocity at the top of the AMBL is given by Eq. (9); with the scaling of Eq. (10), this yields the nondimensional velocity

$$w\left(\frac{H_E}{H}\right) = \frac{1}{2\pi}\frac{H_E}{H}\left[\nabla^2\psi - \frac{gH_E}{f\theta_0LV}\left(1 - \frac{1}{2\pi}\right)\nabla^2T^*\right]. \quad (16)$$

According to the usual conventions of boundary layer theory (Batchelor 2000), $z = 0$ here is understood to apply at the top of the AMBL. Along the meridional boundaries $\psi = q = 0$, while in the zonal direction we use periodic boundary conditions in ψ and q.

In traditional studies of ocean–atmosphere interactions, the vertical integral of the PV source due to heating at the lower boundary is exactly zero (see Kushnir et al. 2002). Heating due to an oceanic front thus cannot directly force a barotropic response in the free atmosphere. In our model, the oceanic SST front does produce a response via the vertical velocity it induces at the top of the AMBL, that is, via the thermal component of the flow in the AMBL.

The nondimensional constant

$$\alpha = \left(1 - \frac{1}{2\pi}\right)\frac{gH_E}{H_aV^2}\left(\frac{k_0}{2f}\right)^{1/2} = \frac{1}{2\pi}\left(1 - \frac{1}{2\pi}\right)\frac{gH_E^2}{H_aV^2} = \frac{1}{2\pi}\left(1 - \frac{1}{2\pi}\right)\frac{H_E}{H_a}\frac{1}{F_r^2} \quad (17)$$

determines the strength of the thermal component of the vertical velocity at the top of the AMBL. It is proportional to the inverse square Froude number of the AMBL. The nondimensional constant

$$\gamma = \frac{1}{2\pi}\frac{H_E}{H_a}\frac{fL}{V} = \frac{1}{2\pi\epsilon}\frac{H_E}{H_a} \quad (18)$$

determines the strength of the mechanical component of the vertical velocity at the top of the AMBL. It is proportional to the inverse of the frontal Rossby number. We see that $\alpha \sim 1/F_r^2$, $\gamma \sim 1/\epsilon$, and both are proportional to H_E/H_a.

The values of ϵ and F_r are given in Table 1; they correspond to a typical oceanic AMBL in midlatitudes. Dimensional analysis yields an order-of-magnitude estimate of $(U_G/L)\nabla^2p$ for the mechanical component and $[gH_ET_a/(f\theta_0L^2)]\nabla^2T$ for the thermal component. Thus, the ratio between the two effects, thermal over mechanical, is $gH_ET_a/(f\theta_0LU_G)$. This ratio is $O(1)$ for $L \simeq 150$ km, using a typical thermal front strength of $T_a = 6$°C and an accompanying scale of the geostrophic zonal velocity U_G of 10 m s^{-1} (as found near the oceanic front in sections 3 and 4), while the other values are as given in Table 1. The mechanical effect becomes more important for larger L, that is, further away from the front.

The numerical scheme is the same as in Feliks (1990) and in Feliks and Ghil (1996). Key features include fourth-order accurate discretization by finite elements in the horizontal (cf. Haidvogel et al. 1980), a second-order Adams–Bashforth scheme in time, and use of a fourth-order Shapiro (1970) filter at every time step.

3. Steady-state solutions

a. The AMBL steady state

First we analyze the steady flow induced in the AMBL by an east–west oceanic front of infinite extent in the

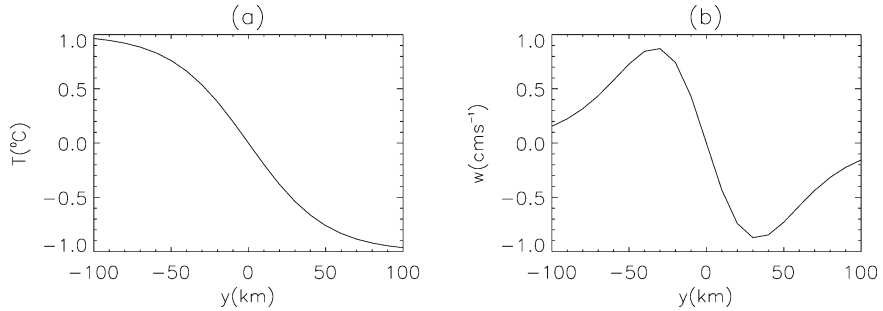

FIG. 2. Cross sections of the oceanic and atmospheric fronts along the y axis for an infinite oceanic front with frontal strength $T_a = 1°C$ and frontal width $d = 50$ km [see Eq. (24)]. (a) The prescribed SST profile; (b) the vertical velocity at the top of the AMBL.

$\pm x$ directions. For such a front, all the SST contour lines are parallel to the x axis and an analytical solution can easily be obtained in the AMBL, as well as in the free atmosphere above. The steady-state solution obtained in section 3b illustrates a number of important features of the time-dependent atmospheric jets obtained in section 4. The meridional, x-independent structure of the SST anomaly field that we prescribe is given by

$$T = -T_a \tanh(y/d), \tag{19}$$

where d is the cross-frontal scale and T_a is the strength of the front. For this temperature profile, the difference in SST between the two water masses separated by the front is $2T_a$, the width of the front is roughly $4d$, and all the AMBL fields in the solution are also independent of x. We only solve for the thermal, SST-induced component of the AMBL flow and will use its vertical velocity $w = w(H_E)$ to drive the free atmosphere (see section 3b).

Since the AMBL model is linear, the thermally induced wind speed is proportional to T_a [see Eq. (9)]. Thus we examine below the case where $T_a = 1°C$ and $d = 50$ km, while $k_0 = 3.3$ m^2 s^{-1}. We show in Fig. 2a a cross section of the SST as a function of y; the thermally induced component of the vertical velocity w at the top of the AMBL is shown in Fig. 2b. In this case, the SST-induced w has its maxima of ± 0.9 cm s^{-1} about 30 km off the axis of the front, to the north and south, respectively, where $\partial^2 T/\partial y^2$ has its maximum; see Eq. (9).

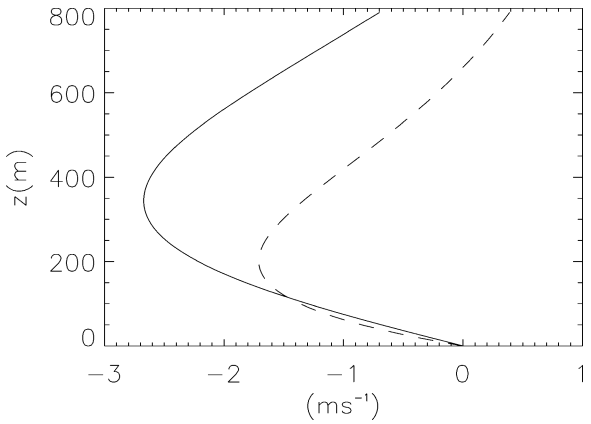

FIG. 3. The analytically obtained vertical profile of the thermal component of u (solid) and v (dashed) in the AMBL at $y = 0$.

In Fig. 3, the vertical profiles of the SST-induced velocity components u and v at $y = 0$ are shown. The maximum of u is at 325 m and that of v is at 200 m. The corresponding vertical profiles of u and v at other points are the same but the amplitude is smaller, since $\partial T/\partial y$ has its maximum at $y = 0$.

The AMBL model used here is linear; that is, the nonlinear advection terms are neglected in the momentum equations (4a) and (4b). The validity of this assumption is evaluated below for a weak front, $T_a = 1°C$, which corresponds to a temperature gradient of 2°C (200 km)$^{-1}$, as well as for a strong front, $T_a = 3.5°C$, which corresponds to a temperature gradient of 7°C (200 km)$^{-1}$. The latter value of the temperature gradient equals approximately the one found across the Gulf Stream and Kuroshio fronts.

In Fig. 4, we examine the different terms of the thermal component in Eq. (4b) versus the nonlinear advection term $v\partial v/\partial y$, which is neglected. The nonlinear term is crudely estimated here from the linear solution (7).

This estimate reaches its maximum at $z = 200$ m and $y = \pm 30$ km. For weak fronts, $T_a = 1°C$, the nonlinear advection term is several times smaller than all the other terms (see Figs. 4a,c), and so it can safely be neglected. For strong fronts, $T_a = 3.5°C$, the nonlinear term is not small at altitudes around 200 m, provided $|y| > 20$ km (see Fig. 4d). It is then comparable to the Coriolis and dissipation terms and to half the pressure term. At lower altitudes, $z < 120$ m, though, the balance is mainly between the pressure and diffusion terms, and the nonlinear term is significantly smaller (see Fig. 4b). At higher altitudes, $z > 300$ m, the main balance is geostrophic, between the pressure and Coriolis terms, and the nonlinear term is again significantly smaller (see Fig. 4b). It is only at intermediate heights, where Ekman balance between all three linear terms prevails, and for strong fronts that the nonlinear term is no longer negligible.

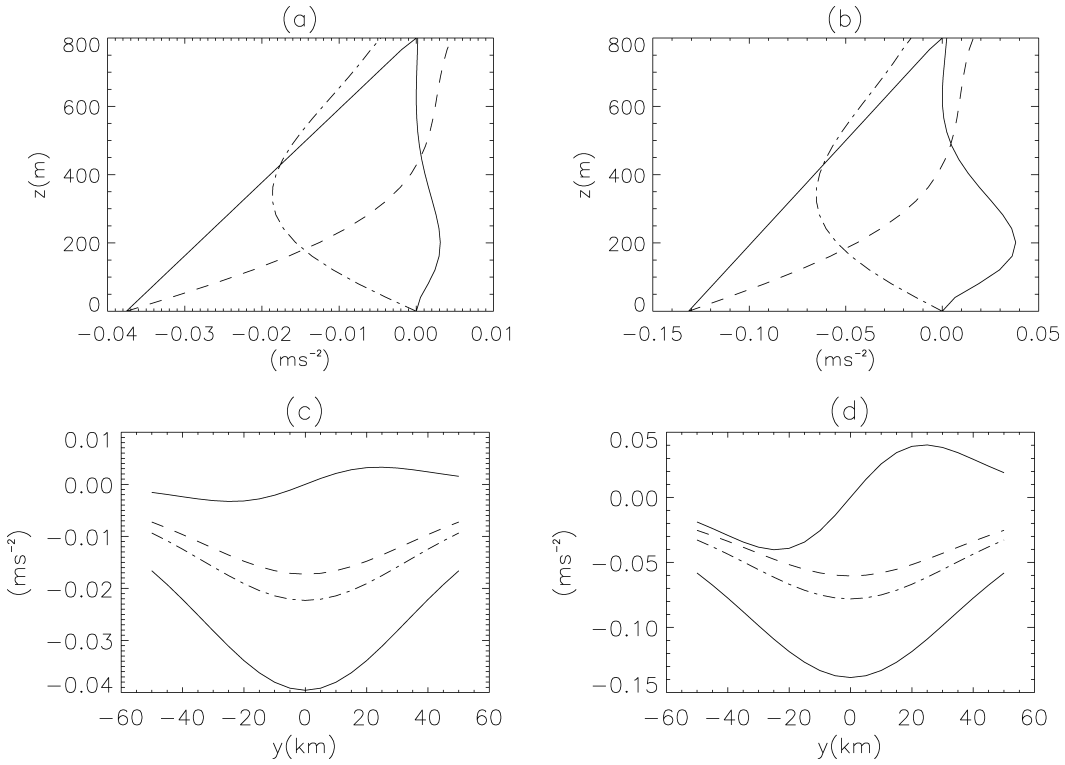

FIG. 4. Different terms in the AMBL momentum equations, Eqs. (4a) and (4b), and the omitted nonlinear term, for the thermal component of an infinite oceanic front: pressure term $-(1/\rho)(\partial p/\partial y)$ (solid), diffusion term $k\partial^2 v/\partial z^2$ (dashed), Coriolis term fu (dashed–dotted), and cross-frontal advection term $v(\partial v/\partial y)$ (dashed–triple-dotted). The vertical profiles at $y = 30$ km: (a) weak front, $T_a = 1$°C; (b) strong front, $T_a = 3.5$°C. The cross-frontal profiles (along the y axis) at $z = 225$ m: (c) weak front; (d) strong front.

There are thus parts of the AMBL where, in the case of strong fronts, the cross-frontal advection term becomes comparable with the smaller one(s) among the linear terms. Still, for an exploratory study like the present one, the linear approximation in the AMBL model seems fairly well justified.

b. The steady flow in the free atmosphere

We now consider, for simplicity, a stationary, x-independent flow in the free atmosphere as well, forced by the vertical velocity $w = w(H_E)$ induced by the infinite oceanic front (19) at the top of the AMBL. The equivalent-barotropic QG model of section 2b is governed by Eqs. (14) and (15). For a simple solution like the one we seek, these equations reduce to

$$\gamma\zeta - \frac{\alpha}{\theta_0}\nabla^2 T = r_H \zeta'', \tag{20}$$

where $(\,\cdot\,)' \equiv d(\,\cdot\,)/dy$, and we use the nondimensional form of the variables.

We are assuming here that the thermal and the mechanical component of the vertical velocity at the top of the AMBL are exactly equal and opposite. This corresponds essentially to assuming that the AMBL has negligible inertia compared not just to the upper ocean (as discussed already in the introduction), but also to the free atmosphere. This assumption is justified a posteriori by the low frequency of the oscillations obtained in the free atmosphere (see section 4 below), when compared to the AMBL adjustment time (see section 1).

The approximate Eq. (9) yields the following balance when neglecting r_H:

$$\zeta_G^* = \left(1 - \frac{1}{2\pi}\right)\frac{gH_E}{f\theta_0}\left(\frac{\partial^2 T^*}{\partial x^{*2}} + \frac{\partial^2 T^*}{\partial y^{*2}}\right); \tag{21}$$

asterisks here indicate dimensional quantities. Neglecting the lateral viscosity r_H in Eq. (20) is also justified a posteriori by the smallness of the diffusion terms in the complete numerical results of section 4. By integrating Eq. (21) with respect to y, from $y = -\infty$ to y^*, we obtain the explicit form for the geostrophic wind at height H_E and meridional position y^*:

$$\begin{aligned} u_G^*(y^*, H_E) &= -\left(1 - \frac{1}{2\pi}\right)\frac{gH_E}{f\theta_0}\left[\frac{\partial T^*}{\partial y^*}(y^*) - \frac{\partial T^*}{\partial y^*}(-\infty)\right] \\ &= -\left(1 - \frac{1}{2\pi}\right)\frac{gH_E}{f\theta_0}\frac{\partial T^*}{\partial y^*}(y^*) \\ &= \left(1 - \frac{1}{2\pi}\right)\frac{gH_E T_a}{f\theta_0}\frac{\operatorname{sech}(y^*/d)^2}{d}. \end{aligned} \tag{22}$$

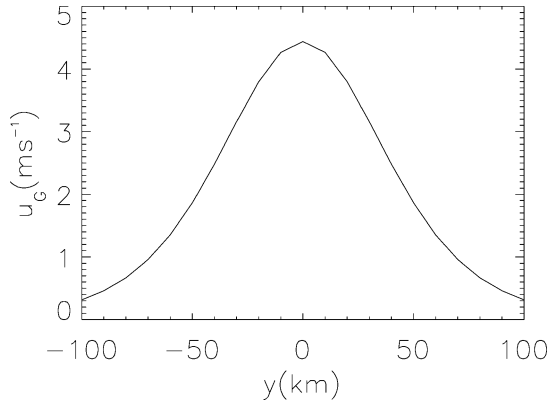

FIG. 5. The analytically obtained meridional, cross-frontal profile of the zonal, along-front velocity $u_G = u_G(y)$ for $T_a = 1$°C.

The geostrophic flow at the top of the AMBL is thus proportional to the oceanic front's strength and to the AMBL height H_E, while it is inversely proportional to the frontal width d. The geostrophic velocity $u_G^* = u_G^*(y^*, H_E)$ is shown in Fig. 5 for a weak front, $T_a = 1$°C. The flow is parallel to the frontal isotherms. The maximum zonal velocity is obtained at $y = 0$ and it equals 4.43 m s^{-1}.

Such a symmetric eastward jet profile is called a Bickley jet (Kuo 1973; Haltiner and Williams 1979, section 4d) and it has two inflection points. The necessary condition for it to experience barotropic instability, in the absence of lateral viscosity and bottom friction, is $-2 < \beta d^2/U_0 < 2/3$, where U_0 is the maximal velocity. In our case, $U_0 = u_G(y^* = 0, H_E) = (1 - 1/2\pi)gH_E T_a/fd\theta_0$, and thus, for $d = 50$ km, it is necessary for U_0 to exceed 0.07 m s^{-1} in order for such a jet to be unstable. To reach this threshold requires, therewith, a much smaller value of T_a than the one that corresponds to the Gulf Stream and Kuroshio fronts, at least in the present, highly idealized case of an infinite oceanic front, without lateral-viscosity effects. We consider both lateral-viscosity and finite-length effects in the next section.

4. Time-dependent solutions

a. Finite-length effects

The case of an infinite oceanic front was treated in sections 3a and 3b analytically, in order to obtain the main characteristics of the thermally induced eastward jet above the front. We turn, therewith, to the somewhat more realistic case, illustrated in Fig. 1, of an oceanic thermal front of finite length. This case represents a better approximation of the thermal fronts associated with the Gulf Stream and the Kuroshio Extension and it will have to be treated numerically. For such an oceanic front, the steady-state solutions differ significantly from the idealized ones given in the previous section, and so does their stability. In section 4b, we carry out a systematic study of the dependence of the finite-front solutions and of their stability on the frontal strength T_a.

To motivate this study, we examine in the present section a strong thermal front that shares certain characteristics with the Gulf Stream and Kuroshio fronts. The dimensional length of the front is $L_x = 600$ km, its strength is $T_a = 3.5$°C, and its width is $d = 50$ km. These values give a temperature change of roughly 7°C (200 km)$^{-1}$ for the hyperbolic-tangent profile of Eq. (19). The other parameters are listed in Table 1.

Spatial patterns (snapshots) of the free-atmosphere solutions will be given from now on in figures with nondimensional units along the axes, as done already with the SST anomaly pattern in Fig. 1. The computational domain size in the main numerical simulations is 4000 km/L × 3500 km/L, with a grid size of $\Delta x = \Delta y = 50$ km/L, and a time step of $T_i \Delta t = 800$ s = 0.009 259 day. The corresponding zonal extent of the atmospheric jet is about 2500 km, which is about half the zonal extent of the computational domain. We will investigate in section 5b the influence of the domain's zonal extent on the solutions.

Due to computational limitations we cannot study the model dynamics as a continuous function of the external parameters, while using a sufficiently small grid size to describe accurately the Laplacian $\nabla^2 T$ of the oceanic thermal front's SST field. To capture, with satisfactory accuracy, the influence of the oceanic front on the evolution of our atmospheric model at the resolution of 50 km, we adjust the strength T_a of the oceanic front, replacing it by $T_* = AT_a$.

We determine the correction factor A so that the vorticity pumped by the AMBL into the free atmosphere on the ''coarse'' grid will be the same as in the analytical solution. The vertical velocity within the first grid cell away from the front is the most important since, for a frontal width of $d = 50$ km, the maximum vertical velocity is obtained at $y \cong \pm 30$ km (see Fig. 2b). To find the correction factor A, we average the analytical vertical velocity w_a in Eq. (15) over a grid cell and compare it with the numerical average of w_a; that is,

$$A = \left[\frac{T(y - \Delta y) - 2T(y) + T(y + \Delta y)}{\Delta y^2}\Delta y\right]^{-1} \times \int_{y-\Delta y}^{y} \frac{\partial^2 T}{\partial y^2}\, dy. \tag{23}$$

The result for the front of interest to us is $A = 2.06$; for example, $T_a = 3.5$°C is thus corrected to $T_* = 7$°C on the grid we use. In the absence of this correction, that is, for $A = 1$, the atmospheric response to a strong oceanic front is quite weak when using $\Delta x = \Delta y = 50$ km/L.

The oceanic front shown in Fig. 1 corresponds to the choice of $T_* = 7$°C and $d = 50$ km/$L = 1$. It has the following spatial pattern:

$$T(x, y) = -T_a \tanh[y/a(x)]; \tag{24}$$

here

$$a(x) = \begin{cases} D, & x \le x_0, \\ d + \dfrac{x - x_1}{x_0 - x_1}(D - d), & x_0 \le x \le x_1, \\ d, & x_1 \le x \le x_2, \\ d + \dfrac{x - x_2}{x_3 - x_2}(D - d), & x_2 \le x \le x_3, \\ D, & x_3 \le x, \end{cases} \tag{25}$$

while $d = 1$, $D = 2000$ km/$L = 40d = 40$, $x_0 = 8$, $x_1 = 12$, $x_2 = 24$, and $x_3 = 28$.

The numerical solutions throughout this whole section, as well as in section 5b, refer only to the free atmosphere: we solve Eqs. (12) and (14) for q and ψ, subject to the prescribed SST field given by Eqs. (24) and (25), as required by the lower boundary condition given by Eq. (15). The model solution within the AMBL is no longer necessary, since it only affects the free atmosphere through the ''thermal pumping'' of the vertical velocity $w(H_E/H)$ in Eq. (15) or Eq. (16).

The spinup process begins from a free atmosphere at rest. An atmospheric jet forms above the oceanic front and two gyres form to either side of this jet: cyclonic to the north and anticyclonic to the south (see Fig. 6, snapshot at $t = 8$ nondimensional units).

At this early stage in the spinup, the jet terminates fairly abruptly, at $x \cong 2000$ km/L, with a zone of diffluence where it splits into the return flows of the two gyres. Subsequently, the jet and the gyres spread eastward due to advection of the momentum by the jet itself (see $t = 24$ and $t = 216$ in the figure). The length of the atmospheric jet is now almost 3000 km/L, more than 4 times the length of the oceanic front (see $t = 216$ and 224). For orientation, $T_i = 0.58$ days (see again Table 1), so that $t = 10$, 100, 1000 in nondimensional time units corresponds roughly to 6, 60, and 600 days.

The growth of the jet's penetration length, and of the zonal extent of the recirculation gyres, as apparent in the first three panels of Fig. 6, is observed in all the other numerical simulations we carried out. It will be explained in section 5.

The jet reaches a maximum zonal speed of 9 m s^{-1} at $t = 216$, mainly near the eastern end of the oceanic front. This speed is about 60% of that predicted by the analytical solution for a steady-state jet and an infinite oceanic front [see Eq. (22)]. This difference is mainly due to momentum advection eastward by the jet itself to regions that are not influenced directly by the intense segment of the oceanic front. So the vorticity and energy pumped through the AMBL over the finite oceanic front region is mainly balanced by this advection, and not by bottom friction, as in Eq. (9), from which (22) was obtained.

At $t = 224$, the zonal jet in the free atmosphere becomes unstable and its eastern end starts to meander. This barotropic instability is due to the jet's strong horizontal shear. The most unstable wave has a length of about 500 km/L. The process of energy transfer from the AMBL that overlies the oceanic front to the jet, and from the jet to the large-scale gyres, continues to maintain the large-scale circulation, non obstante this instability. The energy flux from the jet to the gyres is balanced by friction with the sea surface, through the AMBL, which extracts energy from the gyres at its top.

At later times, eddies detach from the meanders along the downstream, eastern portion of the jet; see, for instance, the panels at $t = 3968$–3992 in Fig. 6. The detached anticyclonic eddies move northward along the eastern tip of the cyclonic gyre, while the cyclonic eddies move southward along the eastern tip of the anticyclonic gyre. These eddies do not seem to penetrate the large gyres themselves, which would eventually weaken their vorticity; instead, they are themselves weakened and washed downstream.

The model was run at $T_* = 7$°C for $t = 10$ yr (i.e., 6293 nondimensional time units) and showed every sign of entering into a statistically stationary regime. We discarded the first 4 yr, so as to eliminate any transients, and examined only the time series of the last 6 yr. In this stationary regime, the solution is aperiodic in time and asymmetric in space. The streamfunction and PV fields were saved every 500 time steps, that is, every 4.63 days.

In order to extract coherent spatiotemporal structures from the streamfunction field, we performed multichannel singular-spectrum analysis (M-SSA; see Plaut and Vautard 1994; Ghil et al. 2002a). To keep the size of the covariance matrices that need to be diagonalized manageable, we used only every second grid point along each axis; that is, 40×35 grid points were used in obtaining the spatial empirical orthogonal functions (EOFs). In the M-SSA, we retained the 10 leading principal components (PCs) of the spatial analysis, which capture 94.6% of the total variance.

The first two eigenmodes in the M-SSA capture, in turn, 26% of this leading spatial variance, that is, 24.6% of the total variance; these two modes have a dimensional period of 68 days. The window width was equal to 30 sampling intervals, that is about 139 days. The fields used in all the time series analyses correspond to averages over each sampling interval; the instantaneous snapshots at these intervals are the ones plotted when discussing the raw data (such as in Fig. 6).

The power spectrum of the mean kinetic energy, defined over a subdomain that encompasses the most intense portion of the jet, is shown in Fig. 7a. It was calculated by the classical Blackman–Tukey lag-correlation method, with 128 lags, and shows a dominant peak at 66–72 days, accompanied by a much smaller peak at 34–38 days. When using other scalar time series extracted from the solution, the 68-day peak is still prominent (not shown).

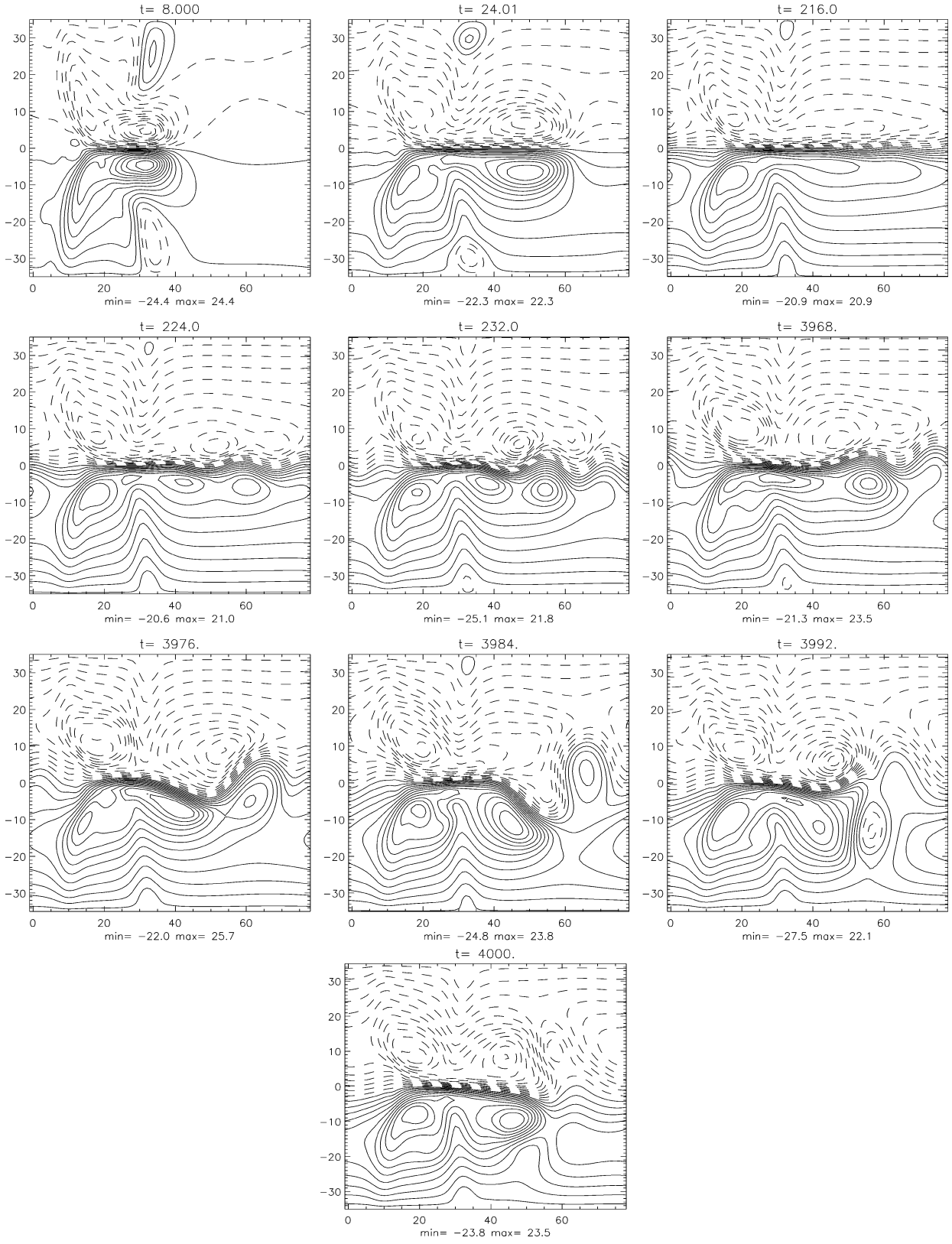

FIG. 6. The numerically obtained free-atmosphere streamfunction (nondimensional) for a finite-length oceanic front. Snapshots shown at unequally spaced times, for a spinup experiment carried out at the adjusted frontal strength $T_* = 7°C$; CI = 2. The adjustment factor A in $T_* = AT_a$ is given by Eq. (23) and equals 2.06.

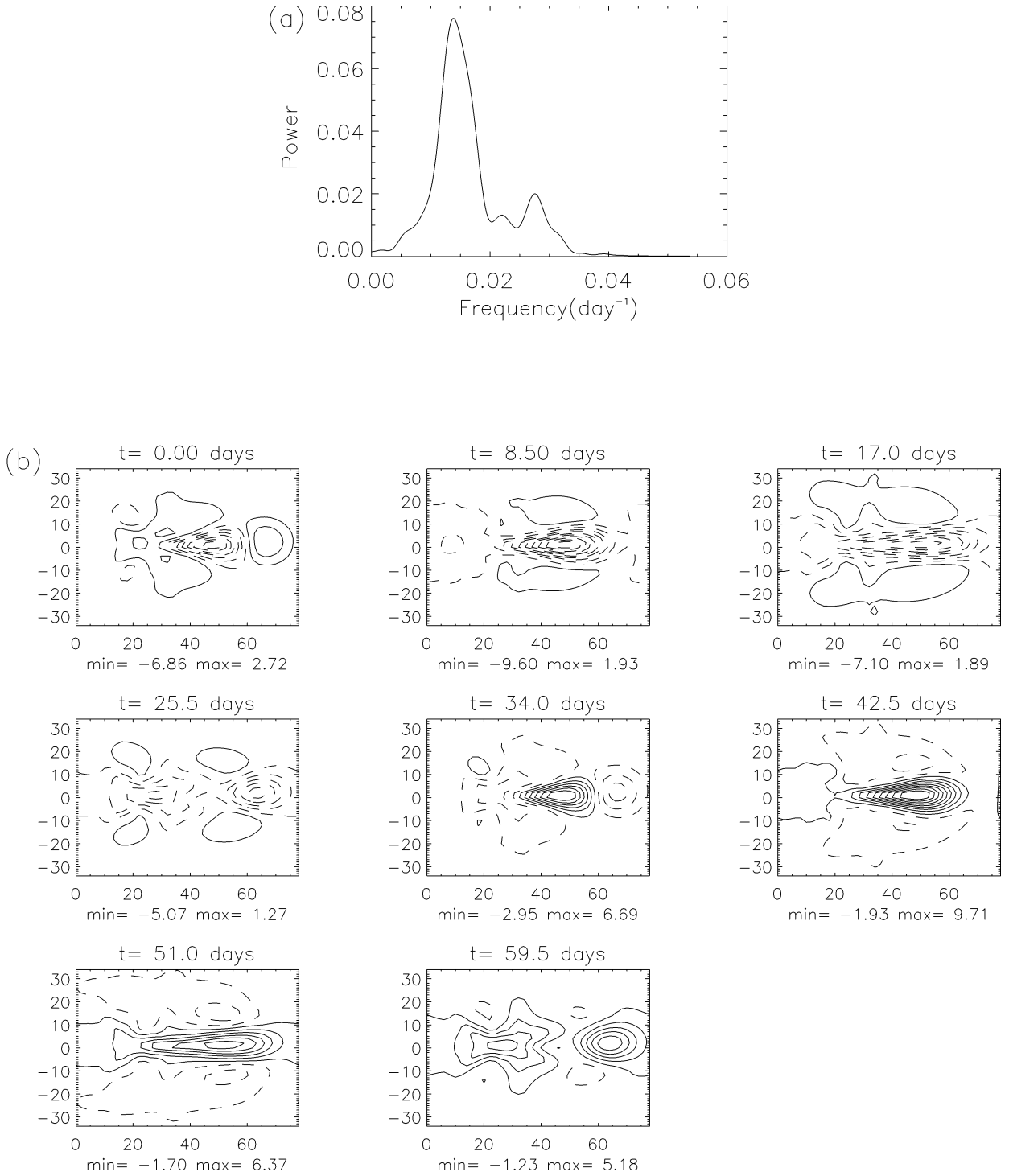

FIG. 7. The 68-day oscillation. (a) The power spectrum of the mean kinetic energy density of the atmospheric jet, computed over a subdomain $\{0 \le x \le 80, -1 \le y \le 1\}$ (in nondimensional units) as the integral of $|\nabla\psi|^2$ divided by the area. (b) The 68-day oscillation obtained at $T_* = 7°C$ is reconstructed using the leading pair of modes and plotted at eight equidistant phases. The plots show the anomalous streamfunction, that is, the difference between the field in the corresponding phase and the mean over the oscillation; phase 1 is in the upper left, and CI = 1 nondimensional unit.

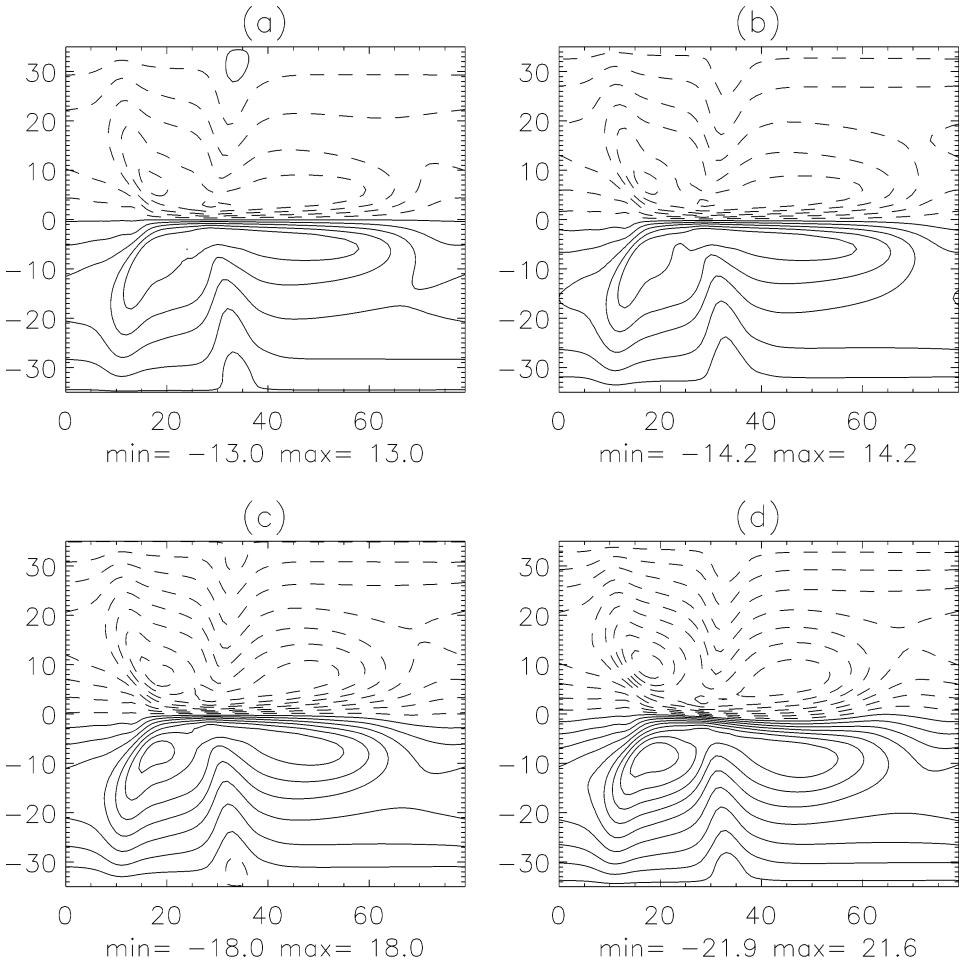

FIG. 8. Model streamfunction field for increasing strength T_* of the finite-length oceanic front: (a) steady-state solution for $T_* = 4$°C; the mean streamfunction for (b) $T_* = 4.5$°C, (c) $T_* = 6$°C, and (d) $T_* = 7$°C; CI = 2.4 nondimensional units.

Eight equally spaced phases of the 68-day oscillation, reconstructed with the two leading M-SSA modes, are shown in Fig. 7b; the compositing of these eight phases follows the methodology of Moron et al. (1998, see their appendix). The mean of the streamfunction field over the last 6 yr of the simulation for $T_* = 7$°C is shown in Fig. 8d.

A negative anomaly begins to develop in the diffluent portion of the jet, near its axis, in phase 1 of Fig. 7b. This anomaly intensifies in place and expands spatially in phases 2 and 3. The negative anomaly then breaks up and decays in phase 4, and a positive anomaly begins to develop through phases 5 and 6, blocking the antisymmetric flow. The positive anomaly, in turn, decays in phase 7 and breaks up in phase 8, making room again for the negative anomaly to replace it.

The initial development of the anomalies is due to linear barotropic instability of the jet's meridional shear, as can be seen more clearly at weaker frontal intensities T_* (see section 4b; not shown here). The phenomena apparent in Fig. 7b are due to the nonlinear evolution of the finite-amplitude, saturated oscillation, with transfer of energy between distinct wavenumbers, as well as between the waves and the basic flow.

We examined the influence of the horizontal resolution on the solution by taking $\Delta x = \Delta y = 25$ km/L; that is, the number of grid points was increased by a factor of 4, from about 5600 points to roughly 22 400. In this case, the correction factor $A = 1.3$ given by Eq. (23) is fairly close to 1.0. The general behavior and characteristics of the solution, for instance, the peaks in its power spectrum, are very similar to those obtained with the grid size of 50 km/L (not shown). We conclude that the relatively coarse grid of 50 km/L is entirely adequate for this study, given a suitably corrected frontal forcing.

b. The LFV's dependence on the oceanic forcing's intensity

We now study the model dynamics as a function of the corrected frontal strength, keeping the frontal width

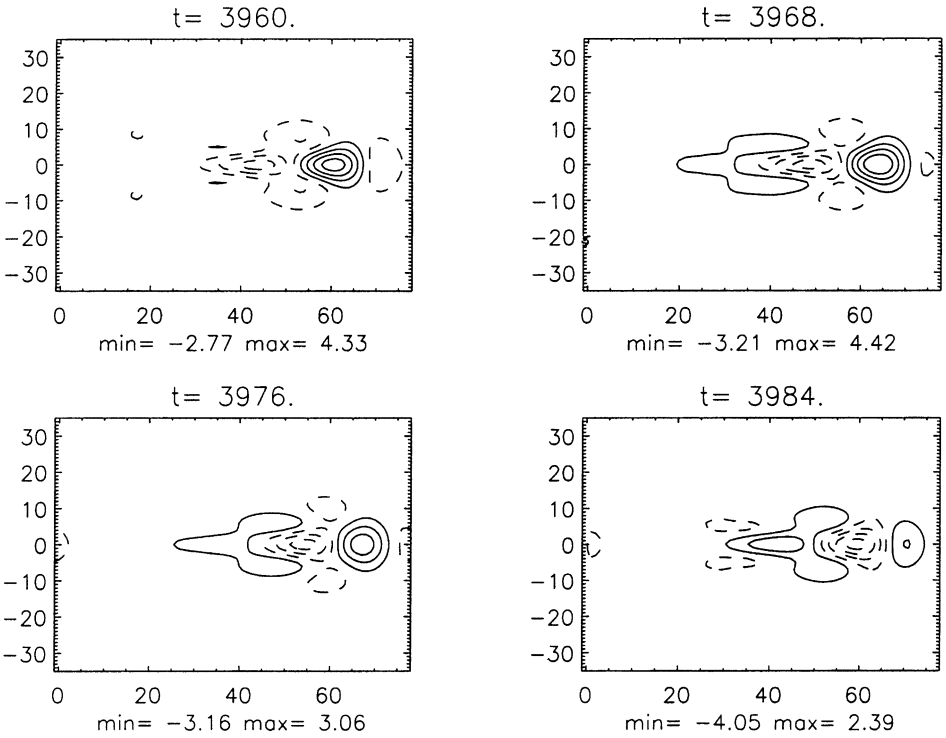

FIG. 9. The spatially symmetric component of the 31-day oscillatory mode at four equally spaced epochs during a half-period for $T_* = 4.5°C$; CI = 1 nondimensional unit.

$d = 50$ km/L fixed in Eqs. (24) and (25). For $T_* \leq 4°C$ the solution in the free atmosphere is steady and exhibits two large, antisymmetric gyres—cyclonic in the domain's northern part and anticyclonic in its southern part—separated by a purely zonal jet (Fig. 8a). This result is quite distinct from the one that would be obtained for an infinite oceanic front, where the streamlines in the free atmosphere would still be parallel to the oceanic isotherms and there would be no recirculation. As discussed at the end of section 3b, the Bickley jet so obtained would be barotropically unstable for such values of T_*.

For $4°C < T_* < 5°C$ the solution becomes periodic in time and asymmetric in space, with a period of 31 days. The linear instability whose saturation gives this finite-amplitude periodic solution is due to locally intense shear in the jet (not shown). For $T_* = 4.5°C$, the mean with respect to time of the streamfunction is still antisymmetric and shown in Fig. 8b. This mean is very similar to the steady solution that obtains for $T_* \leq 4°C$ (Fig. 8a) but it exhibits a slightly more intense circulation.

The anomalies of these periodic solutions, that is, the differences between the instantaneous streamfunction and its time mean, can be decomposed into an antisymmetric and a symmetric component. The antisymmetric component is smaller by an order of magnitude than the symmetric one and plays no significant role in the dynamics for values of the forcing T_* that are close to the onset of the oscillatory instability. The symmetric component is shown in Fig. 9 for a half-cycle of the flow field's evolution over the period of 31 days, at $T_* = 4.5°C$.

The dominance of the symmetric component (see Figs. 7b and 9) is in good qualitative agreement with the rigorous mathematical results of Chen et al. (2004). These authors studied the full partial differential equations governing a forced, dissipative QG jet on a β plane in an x-periodic channel, subject to zonal forcing with a meridionally antisymmetric profile, and showed that Hopf bifurcation occurs through a spatiotemporal mode that has a spatially symmetric pattern and a frequency that is lower than that of the problem's free Rossby waves (i.e., in the absence of forcing and dissipation).

A rough calculation of Rossby wave propagation on a Bickley jet (cf. Kuo 1973; Haltiner and Williams 1979, section 4d) gives periods of the order of several days. These are, indeed, clearly shorter than the 68 days we find for the oscillatory instability here.

In Fig. 9, the anomalies of the symmetric mode at $t = 3960$ have almost exactly the same pattern and the opposite sign when compared to those at $t = 3984$. This mode has a wave pattern of about 1500 km/L in length, which propagates slowly eastward due to advection by the jet. The cellular features of this mode strengthen as they move eastward (see also Fig. 7b), until they reach the diffluence region of the jet, at $x \cong 60$. As the cells continue to propagate further eastward they start to

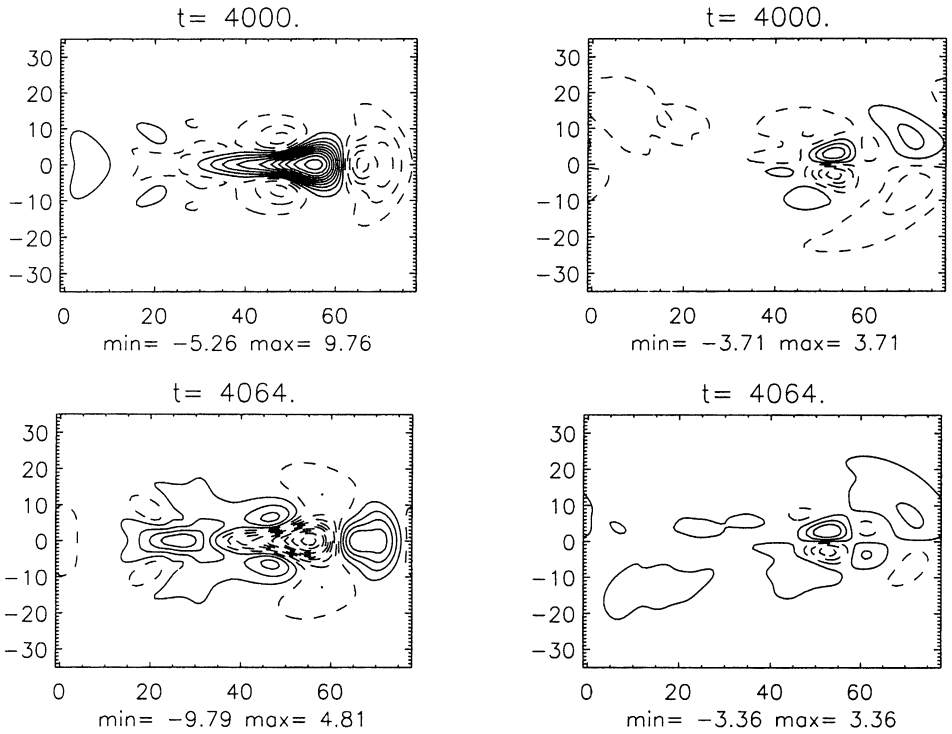

FIG. 10. (left) The symmetric component and (right) the antisymmetric component of the 74-day mode, at two different times, 37 days apart, in the chaotic regime obtained for $T_* = 6$°C; CI = 1 nondimensional unit.

weaken. The intensification of the cells occurs probably by extracting energy from the mean jet over the portion where it is strongest. The subsequent weakening occurs as dissipation is no longer exceeded by the local forcing.

For $T_* \geq 5$°C the solution becomes chaotic. At $T_* = 5$°C the dominant peak in the solution's power spectra has a period of 26 days (not shown). Increasing the oceanic front's intensity further to $T_* = 6$°C, the dominant peak shifts fairly suddenly to a period of 74 days. The time mean of the streamfunction in Fig. 8c is still antisymmetric and resembles the steady solution of Fig. 8a.

The symmetric and antisymmetric components of the dominant oscillatory mode are shown in Fig. 10 at two different epochs, 37 days apart, for $T_* = 6$°C. At this value of T_*, the 74-day mode is quite apparent as nearly periodic spells; the plots in the figure were obtained by sampling these oscillatory spells. The symmetric mode has almost the same pattern, with opposite sign, at these two times (Fig. 10, left-hand side). The meridional scale of the anomaly is about 1000 km/L and the zonal scale is about 2000 km/L. The amplitude of the antisymmetric mode (Fig. 10, right-hand side) is about 1/3 of the amplitude of the symmetric mode, showing that the relative importance of the former tends to grow with T_*.

The case in which the intensity of the oceanic front is even larger, $T_* = 7$°C, was already studied in the previous subsection. The time mean of the streamfunction is still antisymmetric, as seen in Fig. 8d. The spatial extent of significant anomalies in this case is greater: the symmetric mode is still dominant and it covers an area of about 2000 km/$L \times$ 2000 km/L, as shown in Fig. 7b.

From the above solutions we can conclude that, as the oceanic front becomes more intense, the prominent periods in the power spectrum increase. This increase is not monotonic: for $T_* = 4.5$°C the period is 31 days, while for $T_* = 5$°C it is 26 days, but for $T_* = 6$°C the period is 74 days, and for $T_* = 7$°C it is 65 days (see section 3b). In fact, the Hopf bifurcation, which occurs for $4°C < T_* < 4.5°C$, is followed by a second Hopf bifurcation, with a much larger period, just before $T_* = 6$°C. But the period of the limit cycle that arises from either bifurcation decreases monotonically with T_*. The situation is very similar to the one illustrated in Fig. 6.2 of Chen et al. (2003).

Overall, the instabilities with longer periods have also a greater amplitude and spatially larger extent, although the physical mechanism of the instability appears to be the same. The spatially larger extent, as well as the greater amplitude, imply the need to extract more energy from the oceanic front. Since the dissipation is linear, the longer period might be a result of the longer time required for the equilibration of the energy fluxes into and out of the free atmosphere, across the top of the AMBL.

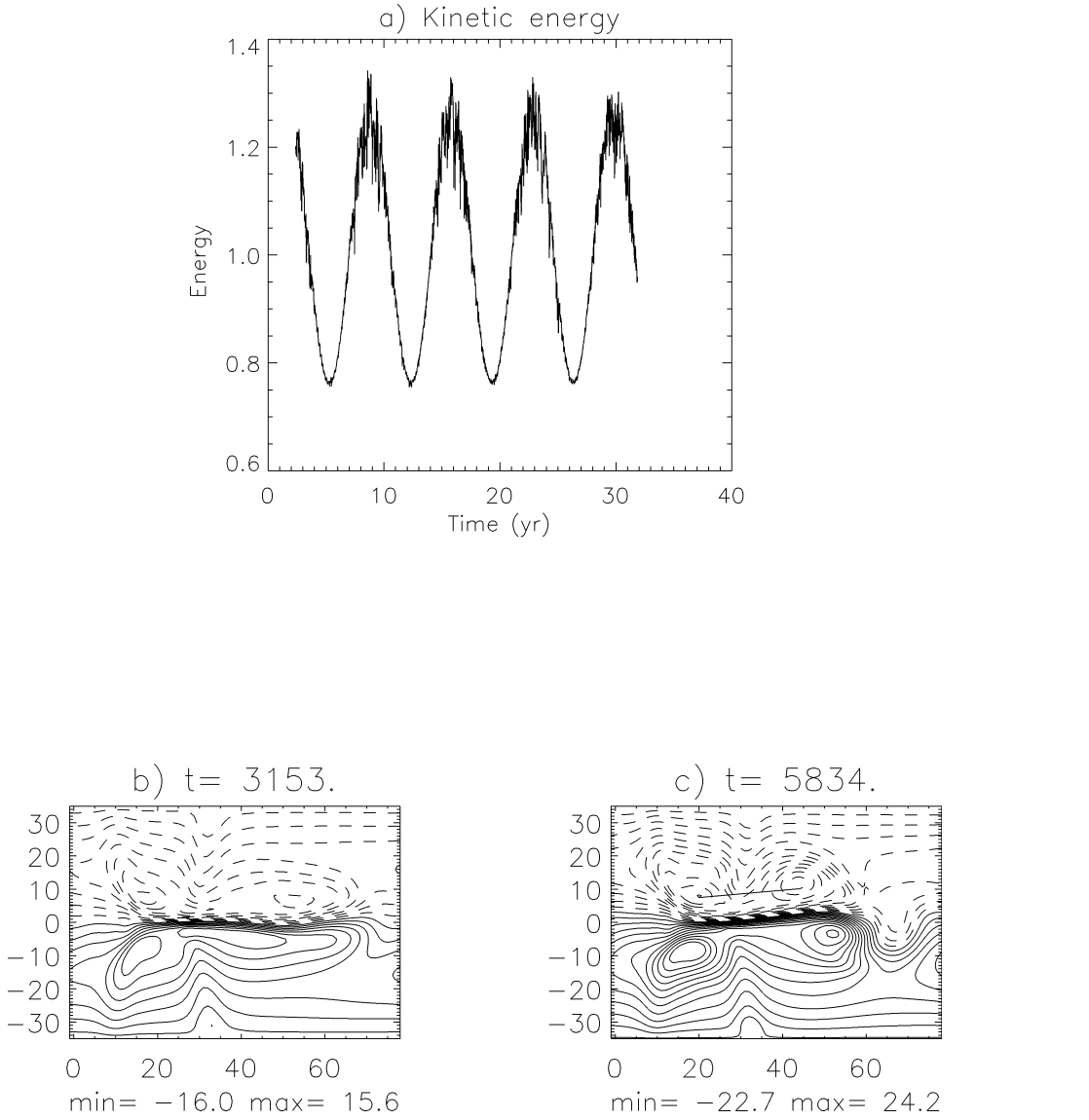

FIG. 11. The evolution of the periodically forced flow. (a) The kinetic energy over the integration domain as a function of time; only three complete cycles of the 7-yr forcing are shown. (b), (c) Streamfunction field for the (b) low-energy phase of the forced solution at $t = 3153$ and (c) high-energy phase at $t = 5834$; CI = 2 nondimensional units.

c. The influence of slow changes in the SST front on the atmospheric LFV

In the following experiment we explore the influence of ultralow-frequency changes on the model atmosphere's LFV. Interannual and interdecadal variability in midlatitude SSTs are known to occur in the North Atlantic and North Pacific (Bjerknes 1964; Deser and Blackmon 1993; Kushnir 1994; Speich et al. 1995; Moron et al. 1998; Chao et al. 2000).

In this experiment the spatial structure of the oceanic front is the same as in Fig. 1 [see also Eqs. (24) and (25) in section 4a]. In the previous experiments, T_a was kept constant in Eq. (24), and hence the corrected value $T_* = AT_a$ was constant in time as well. In the present experiment we allow T_* to be time dependent:

$$T_*(t) = 6 + \sin(\omega t), \tag{26}$$

where $\omega = 2\pi/7\ \mathrm{yr}^{-1}$; thus the perturbation in the frontal strength has a period of 7 yr and an amplitude of 1°C.

The time series of the solution's kinetic energy is shown in Fig. 11a. Two distinct regimes can be identified: a high-energy regime with large fluctuations and a low-energy regime with small fluctuations. In the high-energy regime, the flow in the free atmosphere (Fig. 11c, $t = 5834$) is characterized by a strong zonal jet and vigorous eddies that detach from it, as illustrated

by the succession of snapshots in Fig. 6. In the low-energy regime (Fig. 11b, $t = 3153$), the eddies are weaker and the jet meanders but slightly. The intervals of high and low energy overlap the intervals during which the SST front, and hence $|\nabla^2 T|$, are strong and weak, respectively. The atmospheric jet's intensity is determined by the injection of vorticity into the free atmosphere, and this injection is proportional to $|\nabla^2 T|$ [see Eqs. (14) and (15)].

The model was run with the periodic forcing (26) for 50 yr and only the last 46 yr where analyzed. To describe the spatiotemporal features of the model response, we again used the M-SSA method, as in section 4a. Since we are interested here in periods of several years, the periods of less than 3 months were filtered out by calculating the moving average over this window. After this prefiltering, the 10 leading EOFs of the spatial PC analysis capture 99.5% of the variance. They were analyzed using a window width of 80 times the 3-month sampling interval, that is, of 20 yr.

The only oscillation found to be statistically significant has a period of 7 yr and is captured by eigenmodes (1,2) in the M-SSA analysis. The eight phases of the reconstructed oscillation are plotted in Fig. 12. The figure clearly shows a standing, purely forced oscillation.

The mean of the streamfunction over the last 46 yr (not shown) is quite similar to that obtained for a time-constant forcing with $T_* = 6°C$ (see again Fig. 8c). The anomalies in Fig. 12 are mainly antisymmetric and of one sign on either side of the domain's symmetry axis; the only noteworthy exception occurs as a dipole of variable extent and intensity in the zonal jet's diffluent region. This dominant antisymmetry of the forced, 7-yr oscillation clearly distinguishes it from the self-sustained, internal oscillations, which are dominantly symmetric, for all the intraseasonal periods that we have obtained.

When the anomalous flow is predominantly cyclonic to the north and anticyclonic to the south of the symmetry axis, the anomaly strengthens the mean flow; the opposite is the case when the anomaly has the opposite vorticity. The dipole in the jet's diffluent region grows and decays in extent and intensity in phase with the intensity of the dominant anomaly, while each of its two poles has a vorticity that is opposite in sign to that of the adjacent gyre's anomaly. Hence during high-energy

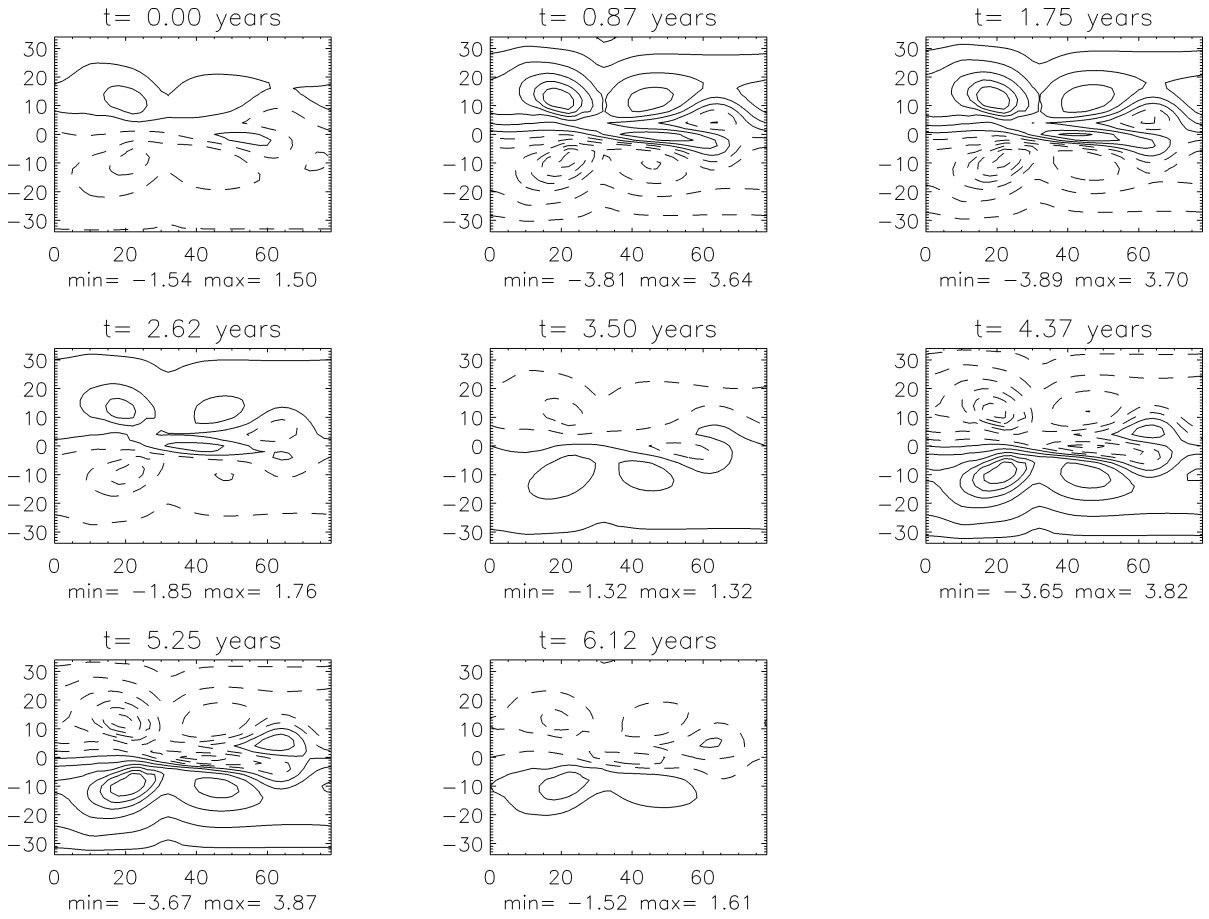

FIG. 12. The reconstructed 7-yr oscillation in eight phases. Phase 1 is at the upper left, and CI = 1 nondimensional unit.

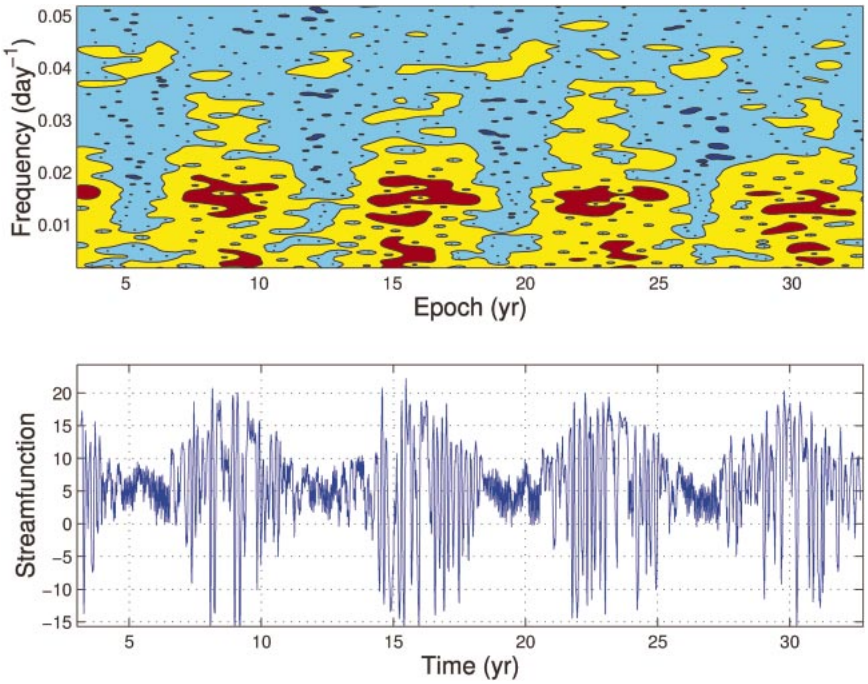

FIG. 13. Evolutive power spectrum of the model's ultralow-frequency behavior: (top) time–frequency diagram of the (bottom) streamfunction time series at grid location (45, 0). The modulus of the short-time Fourier transform $|\int_{-\infty}^{\infty} x(s)h^*(s-t)e^{-2\pi i\nu s}ds|$ in the top has been computed using a Gaussian window $h(s)$ with a width parameter of 4 yr that favors frequency resolution vs time resolution in the Heisenberg principle trade-off. Here, $x(t)$ is the time series being analyzed, $h^*(s)$ is the complex conjugate of $h(s)$, i is the imaginary unit, and ν the frequency. The streamfunction at the bottom is given the nondimensional units.

intervals the jet is shorter than during the low-energy intervals.

We next examine the atmospheric LFV in the high- and low-energy regimes. In the low-energy regime the dominant period is about 25 days, while in the high-energy regime it is about 70 days. The time–frequency diagram of the streamfunction was computed using a short-time Fourier transform, at a point where the LFV is most prominent, and is shown in Fig. 13a; this point is the grid point (45, 0), situated along the jet axis, close to the point of diffluence. The periods of 70–100 days are absent or weak during the low-energy intervals (e.g., years 4–6 and 11–13), while the 25–40-day activity is missing during high-energy intervals (years 7–11 and 13–16). The higher-frequency activity is less pronounced, even when it is strongest, as seen from the time series itself (Fig. 13b).

The spatiotemporal structure of the 25- and 70-day oscillation was reconstructed using M-SSA (not shown). The anomalies are mainly symmetric with respect to $y = 0$ in both cases. The 25-day oscillation in this periodically forced case is very similar to the 30-day oscillation shown in Fig. 9 for the case $T_* = 4.5$°C. Likewise, the 70-day oscillation in the present case is very similar to the 68-day oscillation shown in Fig. 7b for the case $T_* = 7$°C.

Since the externally imposed period of 7 yr is so much longer than the internal periods of about 25 and 70 days, the present results are not surprising. When the front is weak, the 25-day oscillation dominates, as it does for time-constant weak forcing. When the front is strong, the 70-day oscillation is dominant, as it is for time-constant strong forcing.

The situation is thus similar to that found by Strong et al. (1993, 1995) in a QG, barotropic model on the sphere. The model had an intrinsic period of 40 days for Northern Hemisphere winter conditions and one of 15 days for summer conditions. When the forcing was allowed to vary seasonally, the results were essentially the same. It is only when the external and internal periods are closer to each other that interesting nonlinear interactions are expected to arise (Jin et al. 1994, 1996; Tziperman et al. 1994).

5. Concluding remarks

a. Analytical boundary layer model

In this paper we studied the flow induced by an oceanic front (see Fig. 1) in a highly idealized model of the midlatitude atmosphere. A very simple, linear model of the marine boundary layer (AMBL) was coupled to a quasigeostrophic (QG), equivalent-barotropic nonlinear model of the free atmosphere. The extreme sim-

plicity of the model allowed us to focus on a previously neglected but potentially important effect of such a sea surface temperature (SST) front, namely its role as a potential vorticity (PV) source for the free atmosphere. In traditional atmospheric models of ocean–atmosphere interactions, no net PV source due to the lower-boundary heating was present (see Kushnir et al. 2002). In our model, the oceanic front does produce a barotropic response via the vertical velocity it induces at the top of the AMBL, and we found a simple analytical formulation for this vertical velocity, which is proportional to the Laplacian of the SST field.

We also obtained an analytical solution for the flow in the free atmosphere when imposing an oceanic front of infinite length (Figs. 2 and 3). This solution was found to justify the neglect of nonlinear terms in the AMBL model (Fig. 4).

b. Penetration length of the atmospheric jet

We examined next the spinup of the flow in the free atmosphere, when driven by an oceanic thermal front of 600 km in length and a thermal gradient of 3.5°C (100 km)$^{-1}$ (see Fig. 1). The evolution of the flow in this numerical simulation helped motivate the subsequent detailed investigation of the atmospheric flow's dependence on the intensity of the oceanic front. A jet with two large gyres, cyclonic to the north and anticyclonic to the south, spins up from rest over the oceanic front (Fig. 6). At first, the jet is flowing eastward, parallel to the frontal isotherms. This jet strengthens, lengthens, and becomes unstable as the spinup progresses. The most unstable wave has a wavelength of about 500 km. This wave grows to form a large meander and later eddies detach from the downstream end of the jet.

The zonal extent of the atmospheric jet grows during the spinup from hardly more than the 600 km, where the finite-length oceanic front is most intense to several times that length. This growth is found to occur in all our numerical simulations (Figs. 6, 8, and 11b,c). In all these simulations, a limiting value L_x^0 of the jet's zonal extent is found; the length L_x^0 is defined as the distance along the x axis between the point where the maximum speed $U_{\max}$ is attained and the point downstream where the speed falls off to $U_{\max}/e$.

The existence of such a limit to the length of zonal jets follows from the theory of geostrophic turbulence (Charney 1971) in the presence of the β effect (Rhines 1975). Salmon (1998, section 6.3) describes, in particular, the effect of localized midlatitude stirring of an initially quiescent flow in a periodic β channel. In our case, the localized stirring is provided by the finite-length, east–west-oriented front, which induces no net momentum into the atmosphere. Considerations of energy and potential enstrophy conservation predict that the resulting flow is strongly eastward near the latitude of the stirring and weakly westward everywhere else [see Eq. (6.3.19) and Fig. 6.4 in Salmon (1998)].

TABLE 2. Dependence of the atmospheric jet's penetration length on the oceanic front's intensity: $\overline{U}$ is the solution's root-mean-square velocity, $\overline{U}_{\max}$ is the maximum speed of the jet, and k_x is the zonal wavelength. The last two columns compare the theoretical length L_x with the numerically obtained one L_x^0. The value of k_x corresponds to the largest one that is consistent with Eq. (27).

T_*	$\overline{U}$ (m s^{-1})	$\overline{U}_{\max}$ (m s^{-1})	k_x (km^{-1})	$L_x = \dfrac{2\pi}{k_x}$ (km)	L_x^0 (km)
5	1.1	7.5	3.3×10^{-3}	1900	1850
6	1.3	8.3	2.9×10^{-3}	2140	2150
7	1.4	9.2	2.7×10^{-3}	2330	2450

On a β plane, the usual two-dimensional turbulence (Salmon 1998, section 4.8) competes, when $\beta \neq 0$, in transfering energy with Rossby wave propagation. The theoretical value of the eastward jet's maximal extent is given by a comparison of the eddy-turnover time T_U with the Rossby wave period T_ω. This comparison results in the definition of the Rhines scale $k_\beta = (\beta/\overline{U})^{1/2}$, where $\overline{U}$ is the root-mean-square velocity of the flow and a wave vector $\mathbf{k} = (k_x, k_y)$ has length k. The scale k_β separates the domain in wavenumber space where the energy cascades to lower wavenumbers (i.e., longer scales) is effective from that where it is not.

Theoretically, the jet's penetration length in our β channel is limited by the smallest k_x that satisfies

$$\frac{\beta k_x}{k^2} = \overline{U}k. \tag{27}$$

This equality is the same as requiring that $1/T_\omega = 1/T_U$ [see Eqs. (6.3.22), (6.3.23), and (6.3.26) in Salmon (1998)]. From our numerical experiments it follows that $k_y = 2\pi/3500$ km^{-1} in Eq. (27). The resulting value $L_x = 2\pi/k_x$ is compared with the numerically obtained one L_x^0 in Table 2. The excellent numerical agreement, to within 5% of the value predicted by the theory, depends on the exact choice of normalization constant for L_x^0. But the order of magnitude is clearly correct, and L_x^0 does increase with the intensity T_* of the forcing, and hence with $\overline{U}$, as predicted by the theory.

In order to show that our numerical results depend only weakly on the domain's zonal length, we carried out an experiment with a domain size of 8000 km/L × 3500 km/L, so that the zonal length is twice as large as in the previous experiments. We integrate the model with $T_* = 7$°C. In Fig. 14a, the mean state of the run after the spinup is shown, whereas Fig. 14b corresponds to a snapshot of the flow after the spinup interval.

The spinup and the later evolution in this case are very similar to those in the first experiment (Fig. 6). The zonal extent of the jet is still of only about 2000 km and it terminates roughly 4500 km west of the eastern boundary of the domain. The spatial pattern in Fig. 14a is quite similar to that in Fig. 8d, while that in Fig.

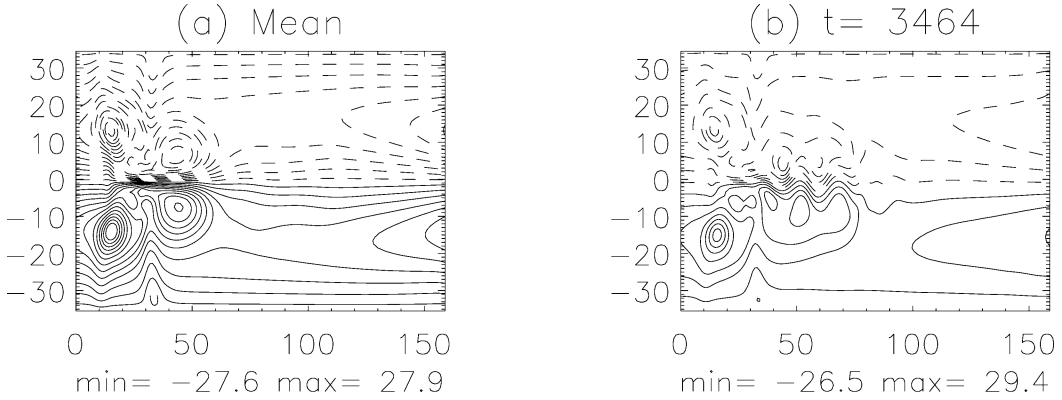

FIG. 14. Streamfunction field for $T_* = 7$°C and a larger domain of 8000 km/$L \times 3500$ km/L: (a) mean streamfunction after reaching statistical equilibrium, as in Figs. 8b–d; and (b) snapshot right after the spinup interval, as in Fig. 6.

14b exhibits just a little more meandering than apparent in the panel labeled $t = 3992$ of Fig. 6.

c. Intraseasonal variability of the jet

We studied systematically the dependence of the model's dynamics on the corrected strength T_* of the oceanic thermal front. The correction was used in the numerical part of the study in order to make the results of this part, at a given horizontal resolution, more directly comparable to the analytical results. For orientation purposes, $T_* = 7$°C corresponds roughly to the strength of the Gulf Stream and Kuroshio surface fronts, when the frontal-width parameter in Eqs. (19) (infinite front) or (24) and (25) (finite front) is $d = 50$ km.

We found that for weak fronts ($T_* \leq 4$°C) the circulation is steady. This circulation has two large antisymmetric gyres with an eastward jet flowing between them (Fig. 8a). As the frontal strength increases (4°C $\leq T_* \leq$ 5°C), the solution becomes periodic in time and asymmetric in space. The period is about 30 days. The asymmetry of the solution is the result of the symmetric pattern of the unstable oscillatory mode being superimposed on the antisymmetric pattern of the steady state that loses its stability (Figs. 8b and 9). This symmetric oscillatory mode has a wavelength of 1500 km. Its amplitude is the largest where the mean jet has its maximum speed, at $y = 0$. The jet's instability is due to the strong shear near the oceanic front.

When the front's intensity is increased to $T_* = 5$°C, the solution becomes chaotic. For $T_* > 6$°C the prominent period is 65–74 days. As T_* increases, the intensity and the spatial scale of the mean, as well as of the anomaly, increase. For instance, for $T_* = 7$°C the scale of the symmetric mode is 2000 km $\times$ 2000 km. The dependence of the solution on the zonal length of the oceanic front and the AMBL's parameters is left for further study.

We thus find in our highly simplified atmospheric model intraseasonal periodicities of 25–75 days (see also sections 4c and 5d). This finding further justifies, a posteriori, the use of an equivalent-barotropic model for the free atmosphere in the present, exploratory study. Indeed, Lau and Nath (1987), among others, showed that midlatitude variability whose time scale is larger than 10 days is associated with equivalent-barotropic vertical structures.

Warner et al. (1990) carried out detailed simulations with a mesoscale model above a wintertime Gulf Stream. At the end of the simulations' 12 h, a vigorous jet develops in the model's lower layers, up to a height of 800 mb. The intensity of this jet depends on the resolution of the SST analysis: it is about 2 m s^{-1} for an SST analysis on a standard operational grid of 380 km, and it is of 7 m s^{-1} when an experimental resolution of 14 km was used in the SST analysis. The latter analysis produced an SST front of about 7°C (50 km)$^{-1}$, even stronger than the strongest oceanic forcing we considered here. The maximum jet velocity we obtain has the correct order of magnitude when compared with the typical 7 m s^{-1} velocity obtained at high resolution in Warner et al. (1990).

The very detailed simulation of Warner et al.'s (1990) mesoscale model is thus in good agreement with the results of our highly idealized atmospheric model, insofar as the effect of horizontal resolution on the strength of the eastward jet is concerned. Warner et al. (1990) also reported stronger vertical velocities and hence relative vorticities (see their Table 1) for their higher-resolution experiment, which is consistent with our linear AMBL results. The shallowness of the strong jet in the detailed mesoscale model (about 1 km from the ground), however, raises the question of the relevance of an equivalent-barotropic upper-air instability of this jet. To verify whether such an instability would still occur in a baroclinic upper-air model, we conducted a preliminary experiment in a two-mode QG model, similar to that of Feliks and Ghil (1996) and of Ghil et al. (2002b), coupled to the same linear AMBL.

In this experiment, we used a 50-km horizontal resolution and a domain size of 4000 km $\times$ 3500 km. The vertical stability profile is chosen so as to yield a depth

of the two layers associated with the two modes that is equal to 2 and 8 km, respectively. The other key parameters are $T_* = 5°C$, $k_0 = 5\ m^2\ s^{-1}$, and $K_H = 5 \times 10^3\ m^2\ s^{-1}$.

The resulting intensity and spatial pattern of the mean barotropic mode (not shown) are quite similar to those obtained when using the equivalent-barotropic upper-air model. After a 10-yr simulation with the baroclinic QG model, and discarding the first 2 yr, we performed M-SSA analysis and found a robust 20-day oscillation. The streamfunction anomalies associated with this oscillatory instability have spatial patterns that are symmetric with respect to the midaxis of the basin (Y. Feliks et al. 2004, unpublished manuscript) and are very similar to those shown in Fig. 9 here for the 30-day oscillatory mode. All the low-frequency instabilities we found so far in the two-mode model exhibit equivalent-barotropic structures. The barotropic instability mechanism of the present paper seems therewith to be physically relevant to more realistic, baroclinic situations as well.

We expect to report in forthcoming work on the way in which the present results are quantitatively modified when modeling in greater detail the shallower, baroclinic phenomena that played a major role in earlier studies of SST anomaly impact on the midlatitude atmosphere (Kushnir et al. 2002). Other effects of interest, in addition to baroclinicity, include that of vertical shear in the free atmosphere's basic flow, as imposed by the prevailing westerlies, and accounting for nonuniform height of the AMBL.

d. Ultralow-frequency atmospheric variability

Interdecadal and interannual variability in midlatitude SSTs has been shown to exist in the North Atlantic and North Pacific (Bjerknes 1964; Deser and Blackmon 1993; Kushnir 1994; Chao et al. 2000). The influence of this SST variability on the atmosphere is not well understood, nor is the associated interaction between the atmosphere and oceans.

We suggest here a possible mechanism for the influence of ultralow-frequency variability in midlatitude oceanic fronts on atmospheric LFV. Varying the intensity of the model's SST front with an interannual period led to periodic behavior in its free atmosphere with the same period (Figs. 11 and 12). The varying frontal strength induced an increase or decrease in the mean atmospheric jet's speed.

Two regimes alternated over the period of the forcing. 1) When the oceanic front and the atmospheric jet are both strong, a high-energy regime is obtained. Large meanders and eddies develop along the jet axis, and the dominant oscillation has a period of about 70 days. 2) When the oceanic front and the atmospheric jet are both weak a low-energy regime results. In this regime, small meanders develop along the jet axis, and the dominant oscillation has a period of about 25 days (Fig. 13).

The mechanism demonstrated in this paper for spinning up the circulation in the free atmosphere is not included in general circulation models (GCMs); this is mainly due to the atmospheric GCMs' low horizontal resolution, with a mesh size larger than 100 km. Since oceanic fronts have a width of about 100 km or less, they cannot be resolved by these models. This shortcoming of current GCMs might provide at least a partial explanation for their difficulties in ascertaining atmospheric effects of midlatitude SST anomalies (e.g., Robertson et al. 2000).

We suggest that the interannual and interdecadal variability of oceanic thermal fronts, such as that of the Gulf Stream and the Kuroshio Extension, can influence the atmospheric flow above via the thermal pumping of the intervening AMBL. The main computational obstacle for exploring further the mechanism found here in large-scale GCMs is the fine horizontal resolution needed to resolve the fronts. One way to overcome this obstacle is to use ''zooming,'' that is, nested grids with high resolution over the region of major oceanic fronts, and low resolution elsewhere.

Acknowledgments. It is a pleasure to thank three anonymous reviewers for interesting and constructive comments. Sandra Topete-Hernandez helped in editing the paper and facilitating communication between the three coauthors on three continents. Our work was supported by a Senior Visiting Fellowship of UCLA's Center for Earth System Research (YF), NSF Grant ATM00-82131 (YF and MG), and DOE Grant DOE DE-FG02-01ER63251 (MG and ES). This is publication 5824 of UCLA's Institute of Geophysics and Planetary Physics.

REFERENCES

Batchelor, G. K., 2000: *An Introduction to Fluid Dynamics.* Cambridge University Press, 615 pp.

Bjerknes, J., 1964: Atlantic air–sea interaction. *Advances in Geophysics,* Vol. 10, Academic Press, 1–82.

Branstator, G. W., 1987: A striking example of the atmosphere's leading traveling pattern. *J. Atmos. Sci.,* **44,** 2310–2323.

Businger, J. A., and W. J. Shaw, 1984: The response of the marine boundary layer to mesoscale variations in sea-surface temperature. *Dyn. Atmos. Oceans,* **8,** 267–281.

Chao, Y., M. Ghil, and J. C. McWilliams, 2000: Pacific interdecadal variability in this century's sea surface temperatures. *Geophys. Res. Lett.,* **27,** 2261–2264.

Charney, J. G., 1971: Geostrophic turbulence. *J. Atmos. Sci.,* **28,** 1087–1095.

Chen, Z.-M., M. Ghil, E. Simonnet, and S. Wang, 2004: Hopf bifurcation in quasi-geostrophic channel flow. *SIAM J. Appl. Math.,* **64,** doi:10.1137/50036139902406164.

Deser, C., and M. L. Blackmon, 1993: Surface climate variations over the North Atlantic Ocean during winter: 1900–1989. *J. Climate,* **6,** 1743–1753.

Dickey, J. O., M. Ghil, and S. L. Marcus, 1991: Extratropical aspects of the 40–50 oscillation in length-of-day and atmospheric angular momentum. *J. Geophys. Res.,* **96,** 22 643–22 658.

Doyle, J. D., and T. T. Warner, 1990: Mesoscale coastal processes during GALE IOP-2. *Mon. Wea. Rev.,* **118,** 283–308.

——, and ——, 1993: Nonhydrostatic simulations of coastal meso-

beta-scale vortices and frontogenesis. *Mon. Wea. Rev.,* **121,** 3371–3392.
Feliks, Y., 1990: Isolated vortex evolution in 2 and 4 mode models. *Deep-Sea Res.,* **37,** 571–591.
——, and M. Ghil, 1996: Mixed barotropic–baroclinic eddies growing on an eastward midlatitude jet. *Geophys. Astrophys. Fluid Dyn.,* **82,** 137–171.
Gallego, B., and P. Cessi, 2001: Decadal variability of two oceans and an atmosphere. *J. Climate,* **14,** 2815–2832.
Ghil, M., and K.-C. Mo, 1991a: Intraseasonal oscillations in the global atmosphere. Part I: Northern Hemisphere and tropics. *J. Atmos. Sci.,* **48,** 752–779.
——, and ——, 1991b: Intraseasonal oscillations in the global atmosphere. Part II: Southern Hemisphere. *J. Atmos. Sci.,* **48,** 780–790.
——, and A. W. Robertson, 2000: Solving problems with GCMs: General circulation models and their role in the climate modeling hierarchy. *General Circulation Model Development: Past, Present and Future,* D. Randall, Ed., Academic Press, 285–325.
——, and Coauthors, 2002a: Advanced spectral methods for climatic time series. *Rev. Geophys.,* **40**, 1003, doi:10.1029/2000GR000092.
——, Y. Feliks, and L. Sushama, 2002b: Baroclinic and barotropic aspects of the wind-driven ocean circulation. *Physica D,* **167,** 1–35.
Giordani, H., and S. Planton, 2000: Modeling and analysis of ageostrophic circulation over the Azores oceanic front during the SEMAPHORE experiment. *Mon. Wea. Rev.,* **128,** 2270–2287.
Haidvogel, D. B., A. R. Robinson, and E. E. Schulman, 1980: The accuracy, efficiency and stability of three numerical models with application to open ocean problems. *J. Comput. Phys.,* **34,** 1–53.
Haltiner, G. J., and R. T. Williams, 1979: *Numerical Prediction and Dynamic Meteorology.* 2d ed. John Wiley & Sons, 477 pp.
Holton, J. R., 1992: *An Introduction to Dynamic Meteorology.* 3d ed. Academic Press, 511 pp.
Hsu, H., 1987: Study of linear steady atmospheric flow above a finite surface heating. *J. Atmos. Sci.,* **44,** 186–199.
Jin, F.-F., and M. Ghil, 1990: Intraseasonal oscillations in the extratropics: Hopf bifurcation and topographic instabilities. *J. Atmos. Sci.,* **47,** 3007–3022.
——, J. D. Neelin, and M. Ghil, 1994: El Niño on the Devil's Staircase: Annual subharmonic steps to chaos. *Science,* **264,** 70–72.
——, ——, and ——, 1996: El Niño/Southern Oscillation and the annual cycle: Subharmonic frequency-locking and aperiodicity. *Physica D,* **98,** 442–465.
Keppenne, C. L., S. Marcus, M. Kimoto, and M. Ghil, 2000: Intraseasonal variability in a two-layer model and observations. *J. Atmos. Sci.,* **57,** 1010–1028.
Kuo, H. L., 1973: Dynamics of quasi-geostrophic flows and instability theory. *Adv. Appl. Mech.,* **13,** 247–330.
Kushnir, Y., 1987: Retrograding wintertime low-frequency disturbances over the North Pacific Ocean. *J. Atmos. Sci.,* **44,** 2727–2742.
——, 1994: Interdecadal variations in North Atlantic sea surface temperature and associated atmospheric conditions. *J. Climate,* **7,** 141–157.
——, W. A. Robinson, I. Blade, N. M. J. Hall, S. Peng, and R. Sutton, 2002: Atmospheric GCM response to extratropical SST anomalies: Synthesis and evolution. *J. Climate,* **15,** 2233–2256.
Lau, N.-C., and M. J. Nath, 1987: Frequency dependence of the structure and temporal development of wintertime tropospheric fluctuations—Comparison of a GCM simulation with observations. *Mon. Wea. Rev.,* **115,** 251–271.
Lee, T., and P. Cornillon, 1996: Propagation of Gulf Stream meanders between 74° and 70°W. *J. Phys. Oceanogr.,* **26,** 205–224.
Lott, F., A. W. Robertson, and M. Ghil, 2001: Mountain torques and atmospheric oscillations. *Geophys. Res. Lett.,* **28,** 1207–1210.
——, ——, and ——, 2004a: Mountain torques and Northern Hemisphere low-frequency variability. Part I: Hemispheric aspects. *J. Atmos. Sci.,* in press.
——, ——, and ——, 2004b: Mountain torques and Northern Hemisphere low-frequency variability. Part II: Regional aspects. *J. Atmos. Sci.,* in press.
Madden, R. A., and P. R. Julian, 1971: Detection of a 40–50-day oscillation in the zonal wind in the tropical Pacific. *J. Atmos. Sci.,* **28,** 702–708.
——, and ——, 1994: Observations of the 40–50-day tropical oscillation—A review. *Mon. Wea. Rev.,* **122,** 814–837.
Moron, V., R. Vautard, and M. Ghil, 1998: Trends, interdecadal and interannual oscillations in global sea-surface temperatures. *Climate Dyn.,* **14,** 545–569.
Neelin, J. D., and W. Weng, 1999: Analytical prototypes for ocean–atmosphere interaction. Part I: Coupled feedbacks as a sea surface temperature dependent stochastic process. *J. Climate,* **12,** 697–721.
Pedlosky, J., 1987: *Geophysical Fluid Dynamics.* 2d ed. Springer-Verlag, 710 pp.
Plaut, G., and R. Vautard, 1994: Spells of low-frequency oscillations and weather regimes in the Northern Hemisphere. *J. Atmos. Sci.,* **51,** 210–236.
Rhines, P. B., 1975: Waves and turbulence on a beta-plane. *J. Fluid Mech.,* **69,** 417–443.
Robertson, A. W., M. Ghil, and M. Latif, 2000: Interdecadal changes in atmospheric low-frequency variability with and without boundary forcing. *J. Atmos. Sci.,* **57,** 1132–1140.
Robinson, A. R., Ed., 1983: *Eddies in Marine Science.* Springer-Verlag, 609 pp.
Rogers, D. P., 1989: The marine boundary layer in the vicinity of an ocean front. *J. Atmos. Sci.,* **46,** 2044–2062.
Salmon, R., 1998: *Lectures on Geophysical Fluid Dynamics.* Oxford University Press, 378 pp.
Saravanan, R., and J. C. McWilliams, 1995: Multiple equilibria, natural variability, and climate transitions in an idealized ocean–atmosphere model. *J. Climate,* **8,** 2296–2323.
Schlichting, H., and K. Gersten, 1999: *Boundary-Layer Theory.* Springer-Verlag, 799 pp.
Shapiro, R., 1970: Smoothing, filtering, and boundary effects. *Rev. Geophys. Space Phys.,* **8,** 359–387.
Simmons, A. J., J. M. Wallace, and G. W. Branstator, 1983: Barotropic wave propagation and instability, and atmospheric teleconnection patterns. *J. Atmos. Sci.,* **40,** 1363–1392.
Speich, S., H. Dijkstra, and M. Ghil, 1995: Successive bifurcations in a shallow-water model, applied to the wind-driven ocean circulation. *Nonlin. Proc. Geophys.,* **2,** 241–268.
Stommel, H. M., 1965: *The Gulf Stream: A Physical and Dynamical Description.* 2d ed. University of California Press, 248 pp.
——, and K. Yoshida, Eds., 1972: *Kuroshio: Physical Aspects of the Japan Current.* University of Washington Press, 517 pp.
Strong, C. M., F.-F. Jin, and M. Ghil, 1993: Intraseasonal variability in a barotropic model with seasonal forcing. *J. Atmos. Sci.,* **50,** 2965–2986.
——, ——, and ——, 1995: Intraseasonal oscillations in a barotropic model with annual cycle, and their predictability. *J. Atmos. Sci.,* **52,** 2627–2642.
Sweet, W., R. Fett, J. Kerling, and P. LaViolette, 1981: Air–sea interaction effects in the lower troposphere across the north wall of the Gulf Stream. *Mon. Wea. Rev.,* **109,** 1042–1052.
Tziperman, E., L. Stone, M. Cane, and H. Jarosh, 1994: El Niño chaos: Overlapping of resonances between the seasonal cycle and the Pacific ocean–atmosphere oscillator. *Science,* **264,** 72–74.
Warner, T. T., M. N. Lakhtakia, J. D. Doyle, and R. A. Pearson, 1990: Marine atmospheric boundary layer circulations forced by Gulf Stream sea surface temperature gradients. *Mon. Wea. Rev.,* **118,** 309–323.
Weng, W., and J. D. Neelin, 1999: Analytical prototypes for ocean–atmosphere interaction at midlatitudes. Part II: Mechanisms for coupled gyres modes. *J. Climate,* **12,** 2757–2774.